Monthly Notices of the ROYAL ASTRONOMICAL SOCIETY

MNRAS **518,** 93–110 (2023)
Advance Access publication 2022 October 13

https://doi.org/10.1093/mnras/stac2921

Shedding light on low-mass subhalo survival and annihilation luminosity with numerical simulations

Alejandra Aguirre-Santaella [1,2]★ Miguel A. Sánchez-Conde,[1,2] Go Ogiya [3,4,5] Jens Stücker [6] and Raul E. Angulo [6,7]

[1]*Instituto de Física Teórica UAM-CSIC, Universidad Autónoma de Madrid, C/ Nicolás Cabrera, 13-15, E-28049 Madrid, Spain*
[2]*Departamento de Física Teórica, M-15, Universidad Autónoma de Madrid, E-28049 Madrid, Spain*
[3]*Institute for Astronomy, School of Physics, Zhejiang University, Hangzhou 310027, China*
[4]*Waterloo Centre for Astrophysics, University of Waterloo, Waterloo, ON N2L 3G1, Canada*
[5]*Department of Physics and Astronomy, University of Waterloo, 200 University Avenue West, Waterloo, Ontario N2L 3G1, Canada*
[6]*Donostia International Physics Center (DIPC), Manuel Lardizabal Ibilbidea, 4, E-20018 Donostia, Gipuzkoa, Spain*
[7]*IKERBASQUE, Basque Foundation for Science, E-48013 Bilbao, Spain*

Accepted 2022 October 8. Received 2022 September 28; in original form 2022 July 27

ABSTRACT

In this work, we carry out a suite of specially designed numerical simulations to shed light on dark matter (DM) subhalo survival at mass scales relevant for gamma-ray DM searches, a topic subject to intense debate nowadays. We have employed an improved version of DASH, a GPU *N*-body code, to study the evolution of low-mass subhaloes inside a Milky-Way-like halo with unprecedented accuracy, reaching solar-mass and sub-parsec resolution. We simulate subhaloes with varying mass, concentration, and orbital properties, and consider the effect of baryons in the host. We analyse the evolution of the bound mass fraction and annihilation luminosity, finding that most subhaloes survive until present, yet losing in some cases more than 99 per cent of their initial mass. Baryons induce a much greater mass-loss, especially when the subhalo orbit is more parallel to the Galactic disc. Many of these subhaloes cross the solar Galactocentric radius, making it easier to detect their annihilation fluxes from Earth. We find subhaloes orbiting a DM-only halo with a pericentre in the solar vicinity to lose 70–90 per cent of their initial annihilation luminosity at present, which increases up to 99 per cent when including baryons. We find a strong relation between subhalo's mass-loss and the effective tidal field at pericentre. Indeed, much of the dependence on all considered parameters can be explained through this single parameter. In addition to shedding light on the survival of low-mass Galactic subhaloes, our results can provide detailed predictions that will aid current and future quests for the nature of DM.

Key words: galaxies: haloes – cosmology: theory – cosmology: dark matter – methods: numerical.

1 INTRODUCTION

There is strong evidence to believe that there should exist something else apart from the matter we are able to observe in the Universe. Indeed, there are completely independent cosmological and astrophysical observations which point that, if our theory of gravity is correct, the mass of the matter we can detect electromagnetically is not enough to explain certain phenomena, but by adding a new matter component, dark matter (DM), it is possible (Bertone, Hooper & Silk 2005; Garrett & Duda 2011; Bertone & Hooper 2018; Aghanim et al. 2020).

Despite our efforts, the nature of the DM is yet unknown. There are three main different yet complementary methods to look for DM: direct production (using collider experiments in particle accelerators), direct detection (that look for traces of interactions between DM and baryonic matter at the laboratory) (Kahlhoefer 2017), and indirect detection (Bertone & Merritt 2005). The indirect detection method aims to observe the radiation (gamma-rays and neutrinos) and antimatter (e.g. positrons) produced by DM annihilation or decay into Standard Model particles which could be detected through spatial or terrestrial observatories, such as H.E.S.S. (Hinton & HESS Collaboration 2004), MAGIC (Flix & MAGIC Collaboration 2004), VERITAS (Weekes et al. 2002), *Fermi*-LAT (Gehrels & Michelson 1999), IceCube (Achterberg et al. 2006), AMS (Battiston 2008), and PAMELA (Picozza et al. 2007). A detection of these annihilation products might give a hint about DM properties (Porter, Johnson & Graham 2011). Moreover, all evidence we have on DM is astrophysical as of today, thus indirect searches are the only ones that have the potential not only to make the necessary connection between the nature of the DM and the astrophysical observations, but also to provide direct information about the actual DM distribution in the Universe.

Standard Λ cold dark matter cosmology predicts a hierarchical procedure for structure formation, starting with low-mass virialized objects, or *haloes*, which later in time merge forming larger structures (Springel, Frenk & White 2006; Frenk & White 2012; Zavala & Frenk 2019). As a consequence, there is a huge amount of low-mass subhaloes inside larger haloes like our Galaxy, the Milky Way (MW). The dwarf satellite galaxies are hosted by the most massive subhaloes, while there are also dark satellites (less massive subhaloes with no stars or gas at all) which do not possess visible counterparts.

★ E-mail: alejandra.aguirre@uam.es

Using cosmological *N*-body simulations with a large number of particles per virialized object and a high time and force resolution makes it possible to study the formation of cold DM haloes and their substructure in the non-linear regime in great detail (Diemand, Kuhlen & Madau 2007; Vogelsberger et al. 2020; Angulo & Hahn 2022). Some of them are done assuming that all the matter is dark, that is, baryons are not included. Hence, they are collisionless *N*-body simulations, and even though they are not so precise near the centre of the galaxies, they give an accurate solution of the idealized problem and are by far the best tool we have to understand structure formation and halo structural properties at present. Hydrodynamical simulations are also available nowadays (Vogelsberger et al. 2014; Fattahi et al. 2016; Sawala et al. 2016), which include baryonic material inside the host, thus being more realistic. None the less, the basic properties of subhaloes such as their abundance, distribution, and structure remain unclear for the less massive subhaloes due to the limited resolution in the simulations (Angulo et al. 2014). These simulations typically output subhaloes of at least one million solar masses (Diemand et al. 2008; Springel et al. 2008; Ishiyama et al. 2021), i.e. 12 orders of magnitude larger than the minimum halo mass expected in many DM scenarios. Also, finite numerical resolution implies that at least some subhaloes will be artificially destroyed in simulations.

Indeed, it is unclear whether small subhaloes will survive the strong tidal forces within their hosts since their accretion times to present (Hayashi et al. 2003; van den Bosch et al. 2018; van den Bosch & Ogiya 2018). Some authors claim that almost all subhalo disruption is of numerical origin and a bound remnant should always survive (van den Bosch et al. 2018; Ogiya et al. 2019; Errani & Peñarrubia 2020; Amorisco 2021; Green, van den Bosch & Jiang 2021; Stücker et al. 2022), while other studies suggest that the abundance of small subhaloes is severely reduced due to the effect of tidal forces and of other dynamical agents such as the presence of baryonic material (Garrison-Kimmel et al. 2017; Kelley et al. 2019; Grand et al. 2021; Grand & White 2021). There is about five times more DM than baryonic matter, hence the first one often governs the dynamics. Baryons are particularly important in the centres of large haloes, where galaxies form.

Both subhaloes hosting dwarf satellite galaxies and dark satellites are known to be excellent targets for gamma-ray DM searches since some of them may be close enough to yield large DM annihilation fluxes at Earth (Ackermann et al. 2015; Coronado-Blázquez et al. 2019a, b). Also, the DM-annihilation flux is related to the annihilation luminosity, which is proportional to the DM density squared. Thus, the clumpy distribution of subhaloes will considerably boost the total DM annihilation in their host haloes, reaching values of up to a factor $\sim$60 for galaxy clusters (Sánchez-Conde & Prada 2014; Moliné et al. 2017; Hiroshima, Ando & Ishiyama 2018; Okoli, Taylor & Afshordi 2018; Ando, Ishiyama & Hiroshima 2019, and references therein). Note that having more resilient subhaloes would impact not only this boost computation but also almost every DM constraint obtained to date, as subhaloes are expected to play a key role in almost every DM target.

Here, we carry out a suite of specially designed numerical simulations to shed further light on subhalo survival at all mass scales relevant for DM searches. Specifically, we have employed the DASH[1] simulation code (Ogiya et al. 2019) to study the evolution of subhaloes inside an MW-like halo with unprecedented accuracy. DASH is a fast tree-code optimized for GPU clusters which features both high performance and scalability. It simulates the dynamical evolution of subhaloes with the *N*-body method and analytically describes the gravitational potential of the host. In this way, computational resources are focused on a single subhalo, which allows its simulation with extremely high force and mass resolution, which would not be possible in standard cosmological simulations. More precisely, we will throw a subhalo inside the host and follow its dynamics under different initial configurations such as concentrations, masses, orbital parameters, and accretion redshifts. We will also analyse the effect of taking into account the baryonic disc in the host potential.

Our work is expected to be particularly relevant for DM searches which, indeed, represent one of our ultimate goals. On one hand, we may get significantly larger DM fluxes at Earth from astrophysical objects, such as entire galaxies or galaxy clusters, if we can prove that a significant amount of small subhaloes survive the tidal forces they undergo since their accretion times till present time. This would also impact the computation of the subhalo boost, which could be now calculated in a more realistic way considering the actual abundance and properties of low-mass subhaloes. On the other, some of the surviving, tiny subhaloes closest to Earth would be excellent DM targets by themselves. In this sense, our suite of simulations and obtained results help enlightening the current debate on whether a considerable amount of subhaloes disrupt due to the tidal forces they experience or, on the contrary, we can still hope to look for them with our telescopes.

The work is organized as follows. In Section 2, we describe the code we have used and the modifications we have implemented for this work. The results of our study are depicted in Section 3, giving special attention to two quantities, the bound mass fraction, and the annihilation luminosity, both for runs without and with baryons. In Section 4, we discuss our main findings and compare them to the results in the companion paper, Stücker et al. (2022), where we present an analytical model that treats tidal stripping in the adiabatic limit to predict lower bounds on the asymptotic remnants of subhaloes. Finally, we conclude in Section 5.

2 SIMULATION MODEL

We simulate the dynamical evolution of a DM subhalo orbiting within the MW potential, which consists of a DM host halo, stellar and gas discs, and a bulge. The subhalo is modelled as an *N*-body system, while a time-evolving analytical potential is employed to model the MW. In this section, we describe our simulation model and parameter choice.

2.1 Subhalo

In this study, we consider subhaloes that do not host any stars, and thus they purely consist of DM. Due to the cosmic UV background radiation, star formation in haloes with a virial mass $\lesssim 10^8$ M$_\odot$ is suppressed and the gas within such haloes evaporates (e.g. Bullock, Kravtsov & Weinberg 2000; Okamoto, Gao & Theuns 2008). While we employ the subhalo mass of $m_{\rm sub} = 10^6$ M$_\odot$ in our main simulations, the simulation results can be, in principle, scaled down to arbitrarily small halo masses (Stücker et al. 2022). Specifically, in this work we have tested subhalo masses down to 1 M$_\odot$ (see Section 3.1.2).

We suppose that prior to accretion, the subhalo is spherical and follows the Navarro–Frenk–While (NFW) density profile (Navarro,

[1]While DASH is actually the name of the simulation library, we are calling the code used in our work this way for simplicity.

Frenk & White 1997),

$$\rho(r) = 4\rho_s(r/r_s)^{-1}(1 + r/r_s)^{-2}, \quad (1)$$

where r represents the distance from the centre of the halo, and ρ_s and r_s are the scale density and radius, respectively. The pair of the structural parameters (ρ_s and r_s) can be derived from another pair of parameters, and we employ a pair of the virial mass,[2] M_{200}, and the halo concentration, c, to specify the internal structure of the DM halo in what follows. The virial mass of the halo is given as

$$M_{200} \equiv (800\pi/3)\rho_{\rm crit}(z)r_{200}^3, \quad (2)$$

where $\rho_{\rm crit}(z)$ is the critical density of the Universe at redshift z, and r_{200} is the virial radius of the halo within which the mean density corresponds to $200\rho_{\rm crit}(z)$. The halo concentration is defined as $c \equiv r_{200}/r_s$.

The initial positions of N-body particles with respect to the centre of the subhalo are stochastically drawn using the acceptance–rejection sampling method (Press et al. 2002). We draw r of a particle based on equation (1) in the radial range of $r = [10^{-4}, 1] \times r_{200,\,\rm sub}$, where $r_{200,\,\rm sub}$ is the virial radius of the subhalo at accretion, and its 3D position vector is specified with a randomly drawn unit vector. Note that the truncation of the density distribution in the initial set-up does not affect the main results as particles in the outskirts will be stripped from the subhalo shortly after accreting into the host (van den Bosch & Ogiya 2018). We stochastically draw the particle energy, e, based on the phase-space distribution function, $f(e)$. Here, $f(e)$ is numerically computed using the Eddington (1916) formula. Then we compute the velocity of the particle, v, with e and the gravitational potential of the subhalo. The subhalo has an isotropic velocity dispersion[3] since $f(e)$ is assumed to depend only on the energy, and we specify the 3D velocity vector of the particle with another randomly drawn unit vector. In isolation, the N-body system keeps the initial configuration for a long enough time.

2.2 The host potential

The host potential is composed of a spherical DM host halo and the MW Galaxy that consists of stellar and gas discs and a spherical bulge. The structural parameters of each component evolve with time, based on the empirical relations from cosmological simulations and observations. We input the masses of the DM halo and baryons and parameters introducing their spatial scales at $z = 0$. These are all summarized in Table 1. The centre of the host potential is fixed at the origin of the coordinate system in the entire simulations, i.e. simulations are performed in the host-centric frame. Note that dynamical friction is absent in our simulations as the host is modelled with an analytical potential. Neglecting dynamical friction is justified for the low-mass subhaloes we explore in this paper, as the deceleration of dynamical friction is proportional to the subhalo mass (Chandrasekhar 1943).

[2]This includes only DM mass, as well as (1) in Table 1, so that the total host mass is smaller in runs without baryons.

[3]While the velocity structure in the halo outskirts is radially biased, that in the halo centre ($r \lesssim r_s$) is almost isotropic (e.g. Wojtak et al. 2009; Navarro et al. 2010). The radially biased velocity structure could enhance the mass-loss rate at the beginning of simulations, when the subhalo outskirt is tidally stripped. However, our model should be fine in the later phase in which the subhalo centre has suffered from the tidal effects.

Table 1. Input parameters for the host potential. They are the values at $z = 0$.

(1)	$M_{200,\,\rm host}$	1.0×10^{12} [$M_\odot$]
(2)	$M_{\rm d,\,stellar}$	4.1×10^{10} [$M_\odot$]
(3)	$R_{\rm d,\,stellar}$	2.5 [kpc]
(4)	$h_{\rm d,\,stellar}$	0.35 [kpc]
(5)	$M_{\rm d,\,gas}$	1.9×10^{10} [$M_\odot$]
(6)	$R_{\rm d,\,gas}$	7.0 [kpc]
(7)	$h_{\rm d,\,gas}$	0.08 [kpc]
(8)	$M_{\rm bulge}$	9.0×10^{9} [$M_\odot$]
(9)	$R_{\rm bulge}$	0.5 [kpc]

Notes. Description for each row: (1) mass of the DM host halo, (2) mass of the stellar disc, (3) scale radius of the stellar disc, (4) scale height of the stellar disc, (5) mass of the gas disc, (6) scale radius of the gas disc, (7) scale height of the gas disc, (8) mass of the bulge, (9) scale length of the bulge. Note that the spatial scale r_s of the DM host halo is determined with equation (2) and the concentration–mass–redshift relation. Parameters taken from Kelley et al. (2019).

2.2.1 *Host halo*

The DM host halo is assumed to be spherical in the entire simulation and is modelled with an analytical NFW potential. The virial mass of the host halo potential grows with the model for the mass assembly history of DM haloes by Correa et al. (2015). The concentration of the host halo is derived with the concentration–mass–redshift relation by Ludlow et al. (2016). These structural parameters are updated at every time-step in the simulation (explained in Section 2.4; see also Ogiya, Taylor & Hudson 2021). Note that the DASH simulations performed by Ogiya et al. (2019) employed a static NFW potential to model the DM host halo.

2.2.2 *The MW potential*

As an important update from the original DASH simulations (Ogiya et al. 2019), our simulations now can include not only the DM host halo but also the baryonic components, the central bulge and stellar and gas discs, of the host potential following the recipe of Kelley et al. (2019). We employ a Hernquist (1990) potential to represent the central bulge,

$$\Phi_{\rm Hq}(r) = -\frac{G\,M_{\rm bulge}}{r + R_{\rm bulge}}, \quad (3)$$

where $M_{\rm bulge}$ and $R_{\rm bulge}$ are the mass and the scale radius of the bulge, respectively. Each of the stellar and gas discs is supposed to be an exponential disc, and the mass, scale radius, and scale height of the exponential discs at the present time are listed in Table 1. Flynn, Sommer-Larsen & Christensen (1996) showed that an exponential disc is well approximated by combining separated Miyamoto–Nagai (MN) discs (Miyamoto & Nagai 1975) whose potential is given as

$$\Phi_{\rm MN}(r, z) = -\frac{G\,M_{\rm MN}}{\sqrt{r^2 + \left(\sqrt{z^2 + b^2} + a\right)^2}}, \quad (4)$$

where $M_{\rm MN}$ is the mass of the MN disc and a and b are the MN disc scale radius and thickness, respectively. Following the prescription by Smith et al. (2015), an exponential disc is approximated with three separated MN discs, and the exponential disc parameters ($M_{\rm d}$, $R_{\rm d}$, and $h_{\rm d}$) are converted to the parameters of three MN discs (three sets of $M_{\rm MN}$, a, and b). Since two exponential discs (stellar and gas) are included in the simulations, we have six MN discs in total.

The mass of the stellar components, i.e. the stellar disc and bulge, increases with time by following the abundance-matching model by Behroozi et al. (2019), as the DM host halo mass grows. The mass ratio between the two is fixed as the ratio at $z = 0$ (9/41, see Table 1). The gas mass also increases with time, based on the stellar mass and the gas mass fraction by Popping et al. (2015). The parameters introducing the spatial scale of the baryon potentials (i.e. the exponential disc scale radius and height, and the bulge scale length) are determined as follows. First, the scale radius of the stellar disc is derived by an empirical relation by van der Wel et al. (2014). Then the others are determined to keep the proportion of the baryonic components, e.g. the ratio of the scale radius of the stellar disc to the scale radius of the gas disc is kept. There is another requirement in the model by Kelley et al. (2019). The time-varying baryon parameters must be matched by the input parameters at $z = 0$. To ensure this requirement, we need three scaling factors,[4] namely, ∼2 for the stellar mass, ∼0.75 for the gas mass, and ∼0.35 for the spatial scale parameters of the baryonic components. They are multiplied by the corresponding parameters. The second scaling factor is within the observed scatter (Popping et al. 2015), while the first (third) one seems to be larger (smaller) than the scatter (van der Wel et al. 2014; Behroozi et al. 2019). The mass evolution of each host halo baryonic component, as well as its mass in form of DM, is shown in the top panel of Fig. 1, while the potential of each component at $z = 0$ is shown in its bottom panel.

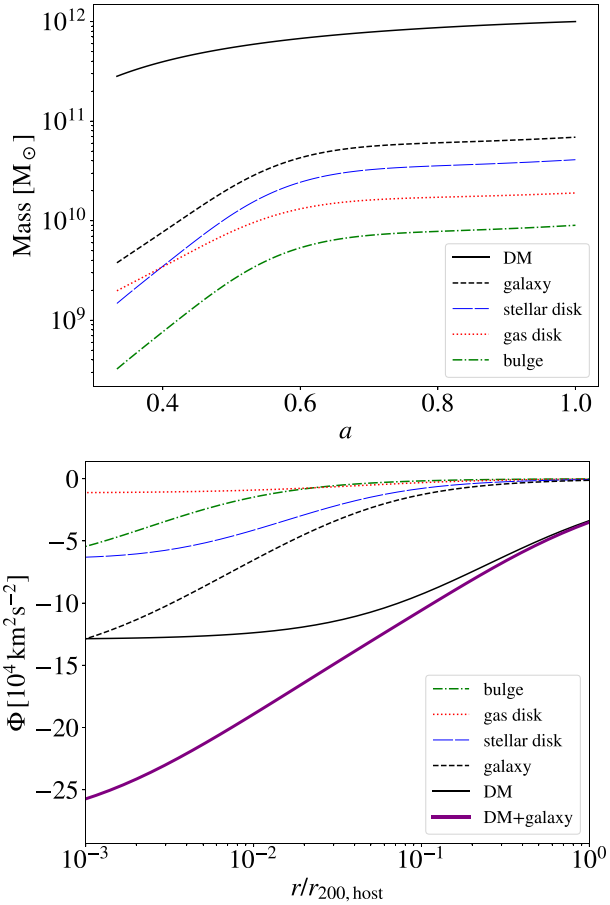

Figure 1. Top: evolution of the various baryon components, similar to Kelley et al. (2019). We can see the evolution of the stellar mass in blue, the gas mass in red, and the bulge mass in green. The sum of these three is the black solid line and accounts for the total baryonic mass, and the DM mass corresponds to the dashed black line. Bottom: values of the potential at $z = 0$ for the different components with respect to the radius, normalized to the host virial radius.

2.3 Subhalo orbit

We take only the potential of the spherical DM host halo into account to set the initial subhalo orbit in the host-centric frame (baryon potentials are ignored in setting the initial subhalo orbit). An advantage of this scheme is that the initial velocity vector of the subhalo is identical when fixing the orbital parameters. The subhalo orbit is characterized with the orbital energy, the angular momentum, and the orbital plane. We employ the following three parameters in this study. The first one describes the orbital energy of the subhalo orbit in the host-centric frame,

$$x_\mathrm{c} \equiv r_\mathrm{c}(E)/r_{200,\mathrm{host}}(z_\mathrm{acc}), \tag{5}$$

where $r_\mathrm{c}(E)$ and $r_{200,\,\mathrm{host}}(z_\mathrm{acc})$ are the radius of a circular orbit of the orbital energy, E, and the virial radius of the host halo at the accretion redshift of the subhalo, z_acc, respectively. The second one controls the angular momentum of the orbit,

$$\eta \equiv L/L_\mathrm{c}(E), \tag{6}$$

where L and $L_\mathrm{c}(E)$ are the actual angular momentum of the subhalo orbit and the angular momentum of the circular orbit of the energy, E. The third parameter is the inclination angle with respect to the Galactic plane, θ.

[4]The evolution of the structural parameters, $M_{200,\,\mathrm{host}}(z)$ and c, is fully specified as a function of redshift by the empirical relations from cosmological N-body simulations. Based on the obtained $M_{200,\,\mathrm{host}}$ and observationally constrained relations, we can get the expected structural parameters of baryons (mass, scale length, and height, etc.) as a function of z. However, it is not guaranteed that the derived baryon parameters are consistent with the input parameters at $z = 0$. To guarantee the consistency, we need to multiply by the mentioned scaling factors.

2.4 Numerical techniques

For N-body computation, we use a code that adopts an oct-tree algorithm (Barnes & Hut 1986) and is accelerated with Graphics Processing Units (Ogiya et al. 2013). The gravitational potential field of particles is smoothed with a Plummer (1911) force softening of $\varepsilon = 0.0003\, r_{200,\mathrm{sub}}$, where $r_{200,\,\mathrm{sub}}$ is the virial radius of the subhalo at accretion. The code employs the cell opening criteria of Springel (2005) with the force accuracy parameter of $\alpha = 0.01$. The position and velocity vectors of particles are updated with the second-order Leapfrog scheme in each N-body iteration, and a time-stepping is determined with the prescription of Power et al. (2003) and is equal for all particles. The centre of the subhalo and its bulk velocity in the host-centric coordinate system is tracked with the scheme outlined in van den Bosch et al. (2018). The evolution of the mass bound to the subhalo is also computed. Only bound particles are considered in drawing the spherically averaged density profile of the subhalo.

2.5 Parameter choices

The high numerical accuracy will enable us to study with great detail subhalo survival and its impact in gamma-ray DM searches using the set of parameters that suit best our purposes. We simulate sub-

haloes with varying mass, concentration, and orbital properties, thus covering the different properties expected in a realistic cosmological scenario. We use six parameters to simulate the subhalo:

(i) The initial subhalo mass, $m_{\rm sub}$. Since we want to study subhaloes not hosting baryonic material, we have chosen $m_{\rm sub} = 10^6$ M$_\odot$. We could use even smaller subhalo masses, but this would increase the computational cost significantly so as to cover a much wider dynamical range. In any case, as we will see later, the results both without and with a baryonic host potential are essentially independent on the subhalo mass.

(ii) The subhalo accretion redshift, $z_{\rm acc}$. We have chosen $z_{\rm acc} = 2$ for most cases since the subhalo accretion distribution in Yang et al. (2011) peaks around that value when considering the host and subhalo masses we are working with. It also gives a reasonable amount of subhaloes crossing the solar Galactocentric radius at some point along their history, i.e. those expected to be most relevant for DM searches (Coronado-Blázquez et al. 2019a).

(iii) The initial subhalo concentration, c. Note that the subhalo is a halo until the moment of accretion, thus the standard definitions of mass and concentration used for haloes are still valid till this happens. As stated in Ludlow et al. (2016), the concentration is around 10 for one million solar masses subhaloes (or haloes) being accreted at $z = 2$. However, the associated scatter can be considerably larger for smaller subhaloes, so we will study concentration values ranging from 5 to 50. This way we would also cover larger concentration values expected for lower mass subhaloes below with $m_{\rm sub} = 10^6$ M$_\odot$.

(iv) Orbital parameters:

(a) The orbital energy parameter, $x_{\rm c}$, as described in Section 2.3.

(b) The orbit circularity, η, as described in Section 2.3.

(c) The orbit inclination angle, θ, as described in Section 2.3. It is only relevant for runs with baryons, when the host spherical symmetry is broken.

Fig. 2 presents the probability distribution of $x_{\rm c}$ and η at the time of subhalo accretion. We employ the fitting function of Jiang et al. (2015) normalized in the 2D parameter space of $x_{\rm c} = [0.5, 2]$ and $\eta = [0, 1]$. As we have a particular interest in subhaloes emitting DM annihilation signals with a detectable flux, subhaloes crossing the solar Galactocentric radius, $R_\odot$, at some point since its accretion are considered. After accretion, the subhalo orbit shrinks as a result of the host growth and the pair of the orbital parameters evolves with time. This effect is taken into account using the model by Ogiya et al. (2021). We find that subhaloes passing $R_\odot$ typically have $x_{\rm c} = 1.2$ and $\eta = 0.3$ at accretion and adopt this pair as our fiducial choice.

Our choice of orbital parameters, together with the typical initial concentration of haloes at a given redshift, as described above, will constitute what will be called our fiducial set of parameters from now on. Nevertheless, we will vary significantly this fiducial set-up in our work by changing the involved parameters to (still reasonable) smaller or larger values, so as to understand the impact of a particular parameter in the results. We summarize both the fiducial setting and the full suite in Table 2.

Finally, we note that our effective mass resolution will depend on the number of particles, N. In particular, $m_{\rm resol} = m_{\rm sub}/N$. We choose N such that we try to ensure convergence of results (see later below) for the particular set of parameters under consideration within our suite, sometimes increasing it significantly to fulfil this requirement from accretion time to present. Some of the adopted values in this work are listed in Table 3. In this same table, we also show the mean inter-particle distance, $d_{\rm ip}$, assuming N particles are homogeneously distributed in a sphere of r_{200}. Some authors advocate $d_{\rm ip}$ sets the minimum value of the softening parameter to ensure the nature of collisionless systems (Melott et al. 1997; Splinter et al. 1998; Romeo et al. 2008). However, in current cosmological N-body simulations, the softening is typically larger than some relevant radii, such as the virial radius of a halo resolved with ∼100 particles, which is $\sim 0.3 d_{\rm ip}$ (Angulo & Hahn 2022). The numbers in Table 3 show that our mean inter-particle distance fulfils that requirement in most cases, i.e. that it is smaller than the softening length. As expected, the lower the subhalo mass the harder to satisfy the condition.

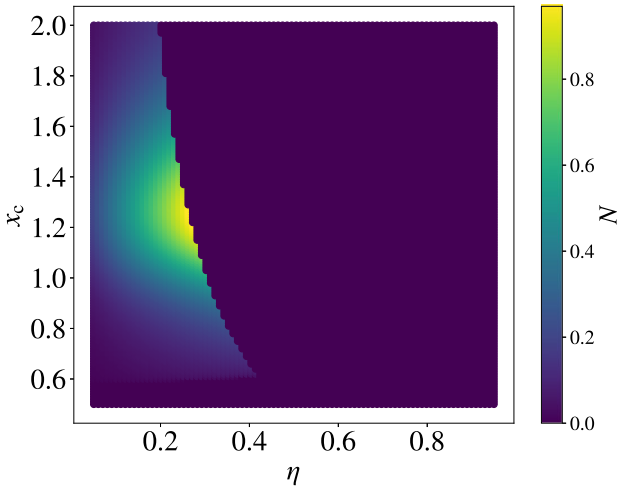

Figure 2. Probability distribution function of the orbital parameters of subhaloes, $d^2p/(dx_c d\eta)$. The fitting function of Jiang et al. (2015) is used. The evolution of the orbital parameters due to the growth of the MW potential is modelled with the prescription of Ogiya et al. (2021). Original pairs (i.e. prior to the evolution) to give an orbit crossing the solar Galactocentric radius, $R_\odot = 8.5$ kpc, between the accretion redshift, $z_{\rm acc} = 2$, and the present time are considered, as such subhaloes are promising targets of DM annihilation signal surveys.

Table 2. Set of parameters used in this work, described in Section 2.5. First column: fiducial parameters. Second column: studied range of each parameter in the full suite.

	Fiducial	Suite
$m_{\rm sub}$[M$_\odot$]	10^6	[1, 10^9]
$z_{\rm acc}$	2	[1,4]
c	10	[5,50]
η	0.3	[0.1,0.8]
$x_{\rm c}$	1.2	[0.8,1.6]
θ [deg]	45	[0,90]

Table 3. Examples of mass resolution (c), mean inter-particle distance (d), and softening length (e) for some subhalo masses (a) and number of particles (b) used in this work. All cases assume $z_{\rm acc} = 2$.

$m_{\rm sub}$[M$_\odot$][a]	N[b]	$m_{\rm resol}$[M$_\odot$][c]	$d_{\rm ip}$ [pc][d]	ε [pc][e]
10^6	2^{18}	3.81	0.16	0.304
10^6	2^{20}	0.95	0.099	0.304
10^6	2^{21}	0.48	0.078	0.304
10^3	2^{20}	0.00095	0.046	0.0304
1	2^{21}	4.77×10^{-7}	0.017	0.00304

3 RESULTS

In this section, we summarize the main findings in our analyses. We have mainly studied two relevant quantities: the bound mass fraction, f_b, which corresponds to the fraction of the initial subhalo mass that remains bound at a given redshift, and the annihilation luminosity, L, which is defined as the integral of the subhalo density profile squared.

3.1 Bound mass fraction

The bound mass fraction comprises the information about how much mass the subhalo has lost when a certain amount of time has passed since its accretion. We define it as the fraction of mass that remains bound at time t with respect to the initial subhalo mass (van den Bosch et al. 2018):

$$f_b = \frac{M(t)}{M_{200,sub}}, \quad (7)$$

where $M(t)$ is the bound mass of the subhalo at time t, and $M_{200,\,sub} = M(< r_{200,\,sub}) = m_{sub}$ is the initial virial mass of the subhalo. This virial radius will not be a good parameter to define the subhalo after accretion, since the mass at the outskirts will be eventually lost and its profile will be consequently truncated.

This quantity allows us to elucidate if the subhalo has been disrupted or if it survives after several orbits. We study f_b for the cases in which the host is made of DM alone as well as the one in which baryons are also included following our prescription in Section 2.2.2. These cases are detailed, respectively, in the next Sections 3.1.1 and 3.1.2. Furthermore, we study the values of f_b that can be trusted in our analyses via the definition of strict convergence criteria in either case, which are nailed down in Appendix A1 for the interested reader.

3.1.1 Non-baryonic case

First, we study the effect that the time evolution of the DM host potential has in the mass-loss process. This is a new feature of our code, neither included in DASH nor shown before. The difference between including this effect or not is illustrated in Fig. 3 for a particular example. A larger subhalo depletion and a larger number of pericentric passages are observed in this more realistic scenario. Most significant changes occur at the pericentre, when a larger fraction of material from the subhalo is stripped by the host (appearing as abrupt 'steps' in this figure). In this particular case, the subhalo whose host evolves loses more mass mainly because it experiences a higher number of pericentric passages. The apocentre is smaller and decreases with time as well. We have checked different cases finding essentially the same results. From now on, we will always adopt the case of an evolving host as the fiducial one, unless specified otherwise.

In Fig. 4, we show f_b as a function of the scale factor, $a = 1/(1+z)$, for different subhalo configurations. In each of them, we vary a parameter among those defining our fiducial set-up specified in Table 2. In particular, in the upper panels of Fig. 4, we show the evolution of f_b for different concentrations and circularities, respectively. From these panels one can see that less concentrated subhaloes at accretion lose mass more quickly, which agrees with the expectations. Also, more radial orbits, i.e. those with smaller η, imply a larger mass-loss. Note that we are comparing different eccentricities here while fixing x_c. Therefore, our orbits with higher eccentricities have smaller pericentres and experience a stronger tidal field. In the lower left-hand panel of Fig. 4 different orbital energy parameter values are displayed. In this case, a smaller x_c leads to a larger number of orbits in the same time interval and thus to a greater mass-loss as well. Finally, the lower right-hand panel shows examples for different accretion redshifts, and we can see that a larger z_{acc} has also the effect of inducing more mass-loss: the subhalo completed more orbits and it initially had a smaller pericentre because the host halo was smaller at earlier cosmic epochs. Indeed, subhaloes accreted at different times landed on different orbits and later-accreted subhaloes have spent less time within the host. We use $N = 2^{18}$ particles in most cases, increasing this number up to $N = 2^{21}$ whenever needed.

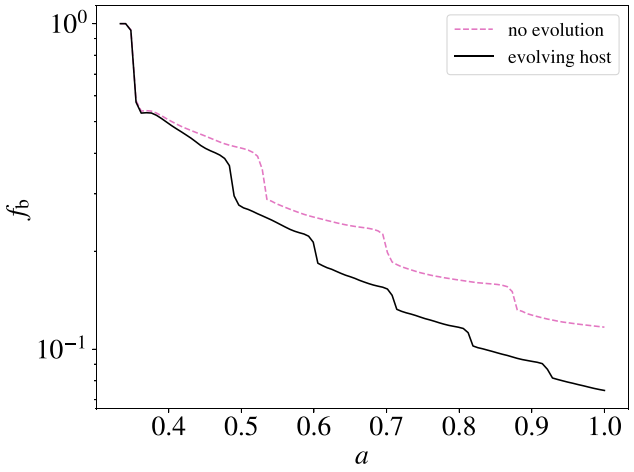

Figure 3. Bound mass fraction as a function of $a = 1/(1+z)$ for a one-million-solar-mass subhalo orbiting a host halo without baryons. We compare two cases: the solid black line corresponds to a scenario in which the DM host potential evolves, while the dashed pink line is for a static host with no evolution. The static mass and concentration are $M_{200,\,host} = 2.82 \times 10^{11} M_\odot$ and $c_{host} = 5.14$, respectively, which are the evolving case initial values, i.e. they are fixed as those at $z = z_{acc}$. In both cases we have used our fiducial set of parameters given in Table 2.

A general picture of f_b results at $z = 0$ in the non-baryonic case, which can be seen in the upper left-hand panel of Fig. 5. In this plot, we fix $x_c = 1.2$ and $z_{acc} = 2$ and vary both the concentration and η parameters. The summary is that subhaloes lose less mass when any of these two parameters is larger. These results are expected to be scale-free when the subhalo mass is small enough. More specifically, results will be identical for ratios $M_{200,\,host}/m_{sub} \gtrsim 10^3$, since self-friction becomes negligible (Ogiya et al. 2019; Miller et al. 2020). Actually, dynamical friction would work more significantly than self-friction in decaying subhalo orbits (Miller et al. 2020). Nevertheless, when considering subhaloes of low enough masses, this drag force would be negligible as well.

3.1.2 Baryonic case

Recent hydrodynamical simulations have shown a significant decrease of the number of subhaloes when baryons are taken into account (Garrison-Kimmel et al. 2017; Kelley et al. 2019; Grand & White 2021; Green et al. 2021). However, this could still be due to numerical artefacts related to insufficient mass and/or force resolution (van den Bosch et al. 2018; van den Bosch & Ogiya 2018). In our work, we want to give an answer to this ongoing debate by performing a variety of simulations including the baryonic component of an MW-size halo as well. Therefore, in order to obtain more realistic simulations we now add baryonic material to the host

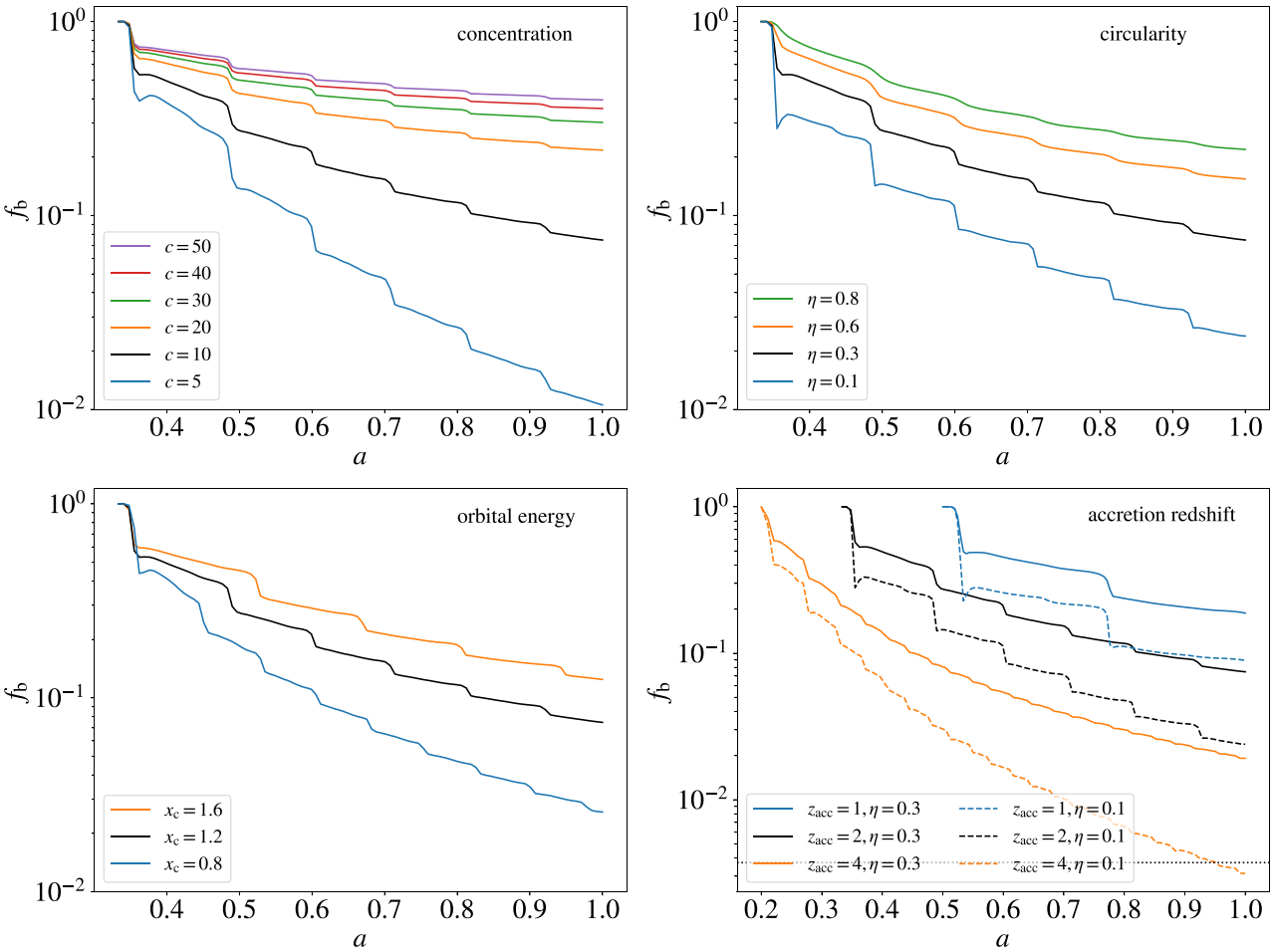

Figure 4. Bound mass fraction, f_b, as a function of $a = 1/(1 + z)$ for different subhalo configurations. Each of them corresponds to a case in which we vary one parameter among those representing our fiducial set-up in Table 2. The latter is depicted as a solid black line in all panels for reference. Upper left-hand panel: different initial subhalo concentrations (c). Upper right-hand panel: different initial circularities (η). Lower left-hand panel: different orbital energies (x_c). Lower right-hand panel: different accretion redshifts (z_{acc}) using two different circularity values. The black horizontal dotted line sets the convergence value for f_b, explained in Appendix A1. When it does not appear, this value is below the chosen y-axis lower limit. Note that f_b is always well above except in the lower right-hand panel, for which no convergence is achieved at present time for the case of $z_{acc} = 4$, $\eta = 0.1$.

potential. This has been done as described in Section 2.2.2, in a way such that the baryonic analytical potential also evolves with time, from accretion until the present.

First of all, we want to understand if also in the case of including baryons the results are scale-free when the subhalo mass is small enough. This was only shown before for the DM-only case (Ogiya et al. 2019, see also Stücker et al. 2022). Our findings are depicted in the left-hand panel of Fig. 6. We can see that results are very similar for masses ranging from one solar mass up to 10 million solar masses. We have also checked the impact of self-friction (Miller et al. 2020) for larger masses. Indeed, this effect starts to be noticeable at $10^8\,M_\odot$ – the orbits become smaller, which leads to more mass-loss – and it is significant for $10^9\,M_\odot$ subhaloes, the difference in f_b at $z = 0$ being a factor $\sim$1.5. In contrast, Ogiya et al. (2019) found no noticeable difference up to $10^9\,M_\odot$ for runs without baryons.

We have also investigated the influence of the orbit inclination angle in subhalo depletion, also studied in Green et al. (2021). Similarly to the latter work, our results, depicted in the right-hand panel of Fig. 6, show that subhaloes with orbits more parallel to the baryonic disc lose more mass. Yet, we report more substantial mass-loss for parallel orbits.[5] Other works (D'Onghia et al. 2010; Garrison-Kimmel et al. 2017) suggested that the mass-loss for a more perpendicular orbit would be greater due to disc shocking when the subhalo suddenly enters or leaves the baryonic tidal field. Here, we find the relevance of this potential effect to be negligible. Instead, we found that another parameter, namely the force accuracy, becomes particularly relevant for parallel orbit runs, since the subhalo in these orbits can deviate from the disc plane after several pericentric passages if the force accuracy is not good enough, which, in turn, causes a small difference in f_b.

In Fig. 7, we compare the impact that adding baryons or not to the host potential has on the bound mass fraction. We adopt an inclination angle of 45 deg in this example as an intermediate choice. As it can be seen, the presence of baryonic material can have a huge impact on

[5]We have checked that using a larger concentration, $c = 20$, as they do, diminishes this difference significantly. We also note that their host potential consists of an NFW DM halo and a single Miyamoto–Nagai disc to account for baryons, both being static, while ours is more elaborated as described in Section 2.2.

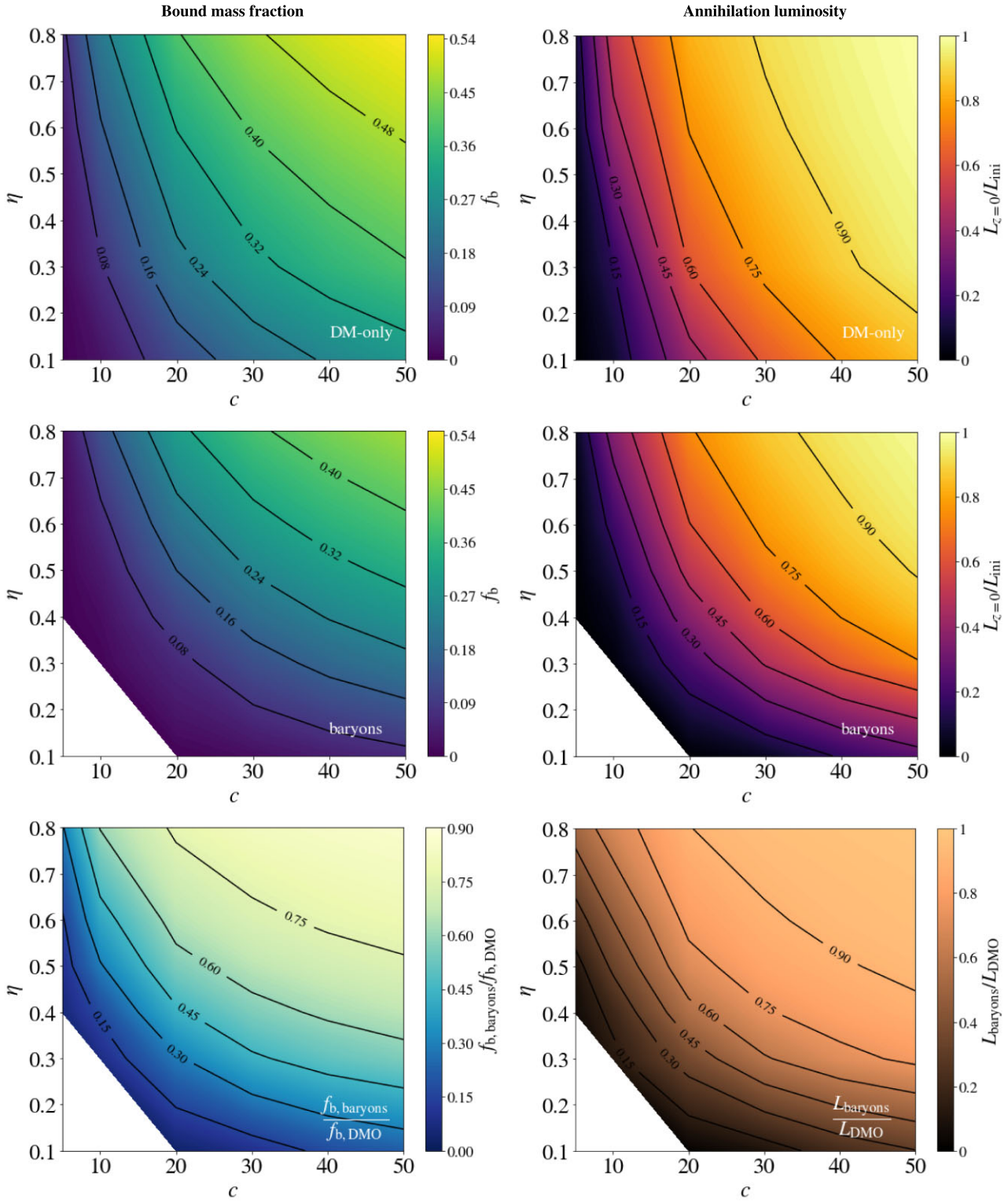

Figure 5. Left-hand panel: bound mass fraction, f_b, at present time for different initial subhalo concentrations and circularities in the non-baryonic case (top) and in case of including baryons (middle). The ratio between the two previous panels, i.e. $f_{b,\,baryons}/f_{b,\,DMO}$ at $z = 0$, is shown in the bottom panel. Right-hand panel: annihilation luminosity results at $z = 0$ varying both the concentration and η parameters, both for the case of excluding baryons (top panel) and with baryons included (middle). The bottom panel shows the ratio between the two previous panels, i.e. $L_{baryons}/L_{DMO}$ at $z = 0$. We adopt a one-million-solar-mass subhalo, with $x_c = 1.2$ and $z_{acc} = 2$ in all cases, and fix the inclination angle of the subhalo orbit to 45 deg in the case of baryons. Non-converged runs are not shown and are the cause of the blank regions in these plots.

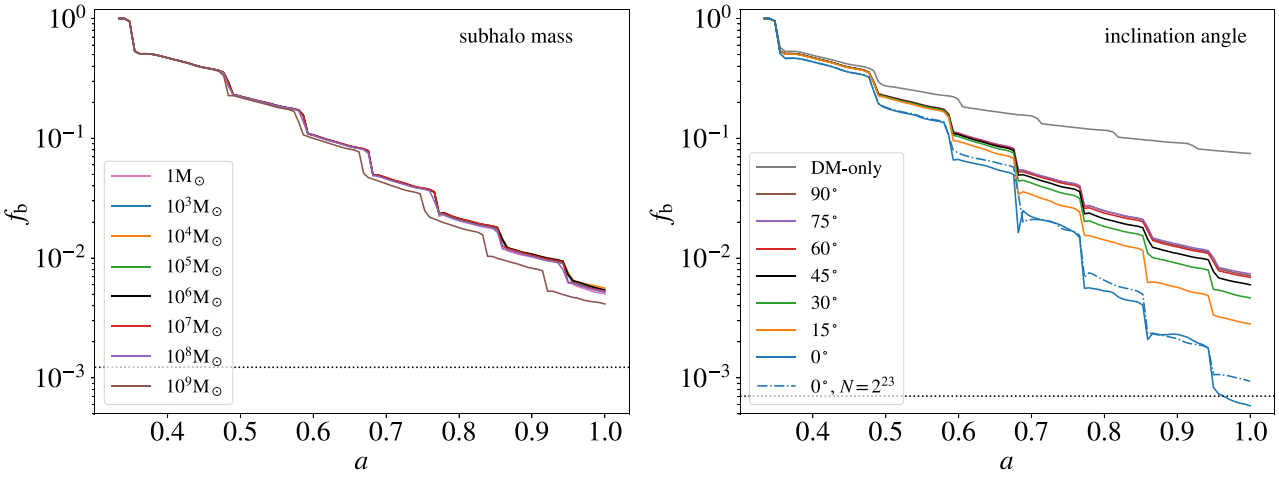

Figure 6. Checks including baryons. Left-hand panel: bound mass fraction, f_b, as a function of $a = 1/(1+z)$ for a subhalo described with our fiducial set of parameters (Table 2), but different initial mass and orbiting an MW-like host with baryonic material. In all cases, the orbit inclination angle with respect to the Galactic disc is 45 deg. Right-hand panel: same as in the left-hand panel, this time for a one-million-solar-mass subhalo orbiting its host with different inclination angles as given in the legend. Zero degree means that the orbit is parallel to the disc, while 90 deg represents a perpendicular orbit. Also shown for comparison are the lines corresponding to the non-baryonic case (grey line) and a run with four times higher resolution (dot–dashed line). In both panels, the horizontal dotted lines represent the convergence limit (for the $N = 2^{20}$ and $N = 2^{21}$ resolution cases in the left- and right-hand panels, respectively; see Appendix A for details).

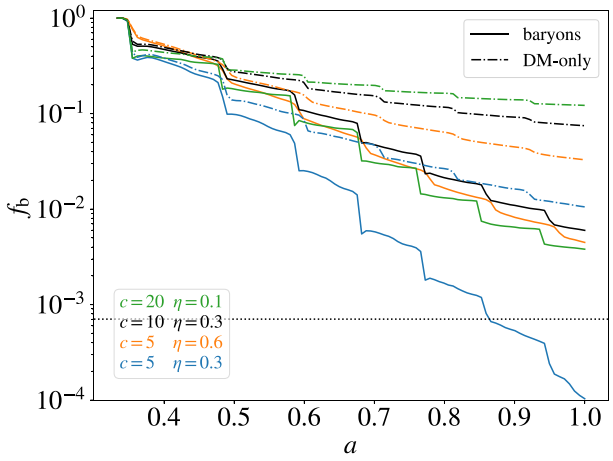

Figure 7. Comparison between adding baryons to the host halo potential or having only DM, for both different concentration and orbital circularity values. The fiducial set-up of Table 2 is shown as a black line. Non-baryonic runs are depicted as dash–dotted lines, while baryonic ones are in solid. The black dotted horizontal line corresponds to the convergence limit; see Appendix A. In all cases, we set $x_c = 1.2$, $z_{acc} = 2$, and $m_{sub} = 10^6 M_\odot$. When baryons are included, the inclination angle is 45 deg.

the subhalo depletion, especially when the pericentre of the orbit is smaller (e.g. decreasing η while fixing x_c). This typically leads to a much smaller f_b for the same time after accretion when compared to the non-baryonic case. Indeed, Fig. 7 shows that some non-baryonic runs with smaller η but larger c can lead to comparatively less mass-loss, while this is not necessarily the case when baryons are included.

A general picture of f_b results at $z = 0$ for the runs including baryons can be seen in the middle left-hand panel of Fig. 5. In this plot, we fix the inclination angle of the subhalo orbit to 45 deg, adopt $x_c = 1.2$ and $z_{acc} = 2$, and vary both the concentration and η parameters. Again, we conclude that subhaloes lose less mass when any of these two last parameters is larger. We note that we cannot achieve numerical convergence for a few cases in our grid,[6] although we do for most of them. An example of the latter can be actually seen as the blue solid line in Fig. 7 as well. The lower left-hand panel of Fig. 5 shows the ratio between baryonic and DM-only runs, and confirms again the larger impact of baryons, especially for subhaloes in more radial orbits. We find the largest differences in the lower left area for the lowest c and η values considered. Besides, on the bottom right corner, where c is large but η is small, this ratio reaches values $\sim$0.25, while the ratio is $\sim$0.3 on the upper left corner. When both c and η are large (upper right area), both values are similar.

3.2 DM annihilation luminosity

Studying the annihilation luminosity of Galactic subhaloes is essential to understand their potential as targets for gamma-ray searches (Ackermann et al. 2012; Strigari 2013; Hooper & Witte 2017). For instance, current DM constraints obtained from the scrutiny of unidentified gamma-ray sources in search of potential subhaloes with no visible counterparts depend, in the first place, on the number of detectable subhaloes predicted from a combination of simulations and instrumental sensitivity (Coronado-Blázquez et al. 2019a, 2021, 2022). More specifically, these DM constraints would be overly optimistic if a significant fraction of subhaloes in the solar vicinity disrupt or lose a significant fraction of their luminosity. Having more resilient subhaloes than those in current simulations would also impact the mentioned DM constraints, this time in the opposite way. Thus, for these studies it is important to have robust predictions of the number of subhaloes, probably down to scales as low as 1000 solar masses (Coronado-Blázquez et al. 2019a). In particular, knowing both the precise abundance

[6] We have tried to improve the convergence using different values of N, up to 2^{21}, but did not succeed. We note though that enlarging N even more drastically should allow to reach a convergent run in the end for most cases; however, the computational resources needed to do so were too expensive.

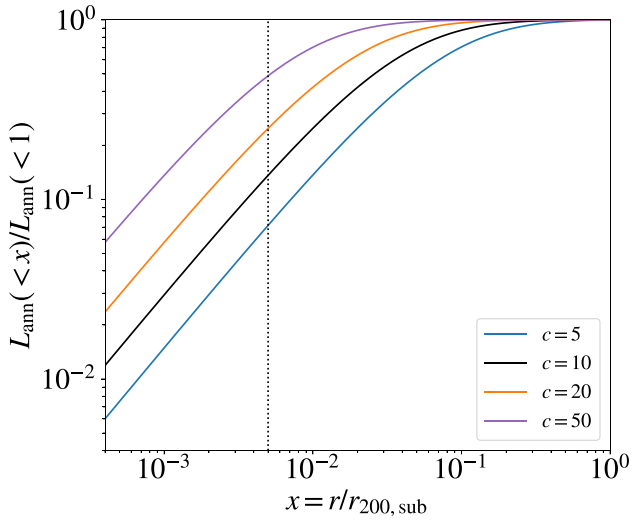

Figure 8. Fraction of the total annihilation luminosity in the region contained inside a radius r, normalized to the subhalo virial radius, for different initial subhalo concentrations. The black dotted line corresponds to the relaxation radius for $N = 2^{24}$ particles, as indicated in Section 3.2 and explained in Appendix A2.

and radial distribution of the subhalo population within an MW-like host would be of utmost importance, not only from a purely cosmological perspective and for current DM constraints, but also e.g. to understand the role of subhaloes for the so-called subhalo annihilation boost (Sánchez-Conde & Prada 2014; Moliné et al. 2017; Ando et al. 2019).

The way to compute the subhalo luminosity is via the radial density profile $\rho(r)$; more specifically, we define the annihilation luminosity in our study as the integration of the DM density profile squared: $L = \int_V \rho^2(r)\,\mathrm{d}V$.[7] The fraction of this annihilation luminosity that reaches the Earth and we can potentially measure with our telescopes is the annihilation flux. We note, however, that the latter cannot be predicted without knowing the exact distance between the subhalo and us.

The fraction of the annihilation luminosity contained inside a normalized (sub)halo radius x, adopting an NFW DM density profile, is shown in Fig. 8 for different initial subhalo concentrations. It can be seen that, even for small concentration values, more than 10 per cent of the total luminosity is inside 1 per cent of the virial radius, and can be more than half for larger concentrations. Therefore, the lack of numerical resolution in the innermost part of the subhalo together with the effect of particle relaxation (explained in detail in Appendix A2) makes the study of the annihilation luminosity a difficult task. Indeed, no particle data are available inside 0.1 per cent of the initial virial radius of the subhalo, and we lose some of these inner particles – up to 1–3 per cent of the initial virial radius, depending on N – after several pericentric passages.[8] This happens specially when the initial concentration is small. To shed further light on this potential issue for annihilation luminosity, we have analysed the change in the density profile of a subhalo as the number of particles increases, and found that the inner cusp remains when N is large enough ($N \gtrsim 2^{22}$; see Fig. A4), but becomes a core when it is not. This implies a significant, non-physical luminosity loss. To solve this problem, we reconstruct the inner cusp in each snapshot in a semi-analytical way by adopting the prescription in Green & van den Bosch (2019). In particular, we integrate this semi-analytical function from $x = 5 \times 10^{-3}$ (i.e. the smallest radius for which we explicitly proved it to be accurate) up to the corresponding relaxation radius, and then we trust the data beyond that point. Full details of this cusp reconstruction can be found in Appendix A2. We note that our particular choice of minimum integration radius in the computation of the annihilation luminosity yields conservative results. Integrating the profile down to a radius smaller than the adopted $x = 0.005$ would indeed lead to larger $L/L_{\rm ini}$ values (e.g. up to a factor 2 for our fiducial case).

In Fig. 9, we show the evolution of the annihilation luminosity normalized to its initial value at accretion, $L/L_{\rm ini}$, as a function of the scale factor, $a = 1/(1+z)$, for different subhalo configurations.[9] In each panel of this figure, we vary one single parameter with respect to the fiducial set-up of Table 2. The first four panels show runs without baryons. In particular, in the upper panels we show the evolution for different concentrations and circularities, respectively. We conclude that less concentrated subhaloes at accretion get reduced to a smaller fraction of their initial luminosity (by e.g. a factor ∼4 in the fiducial case), which is in tune with expectations. Also, more radial orbits, i.e. those with smaller η, experience the same effect. Note that we are comparing different eccentricities here while fixing $x_{\rm c}$. Therefore, our orbits with higher eccentricities have smaller pericentres and undergo a stronger tidal field. In the middle left-hand panel, different orbital energy parameters are displayed. We observe that smaller $x_{\rm c}$ values lead to a larger number of orbits in the same time interval and a larger luminosity decrease as well. The middle right-hand panel shows results for different accretion redshifts: larger $z_{\rm acc}$ also allows for more orbits and a smaller pericentre (because the host halo was smaller at younger cosmic epochs) and thus the luminosity is significantly lower at present for earlier accreted subhaloes. A comparison between runs without and with baryons is shown in the lower left-hand panel. Notice again that η becomes relevant when baryons are included, since a small value induces a greater change in the luminosity. Lastly, the lower right-hand panel shows the luminosity for orbits with different inclination angles with respect to the baryonic disc, confirming that subhaloes in parallel orbits become less luminous after several pericentric passages.

A general picture of annihilation luminosity results at $z = 0$ varying both the concentration and η parameters can be seen in Fig. 5, both for the case of excluding baryons (top right-hand panel) and with baryons included (middle right). We adopt $x_{\rm c} = 1.2$ and $z_{\rm acc} = 2$ in all cases, and fix the inclination angle of the subhalo orbit to 45 deg in the case of baryons. As in the case of $f_{\rm b}$, we do not reach numerical convergence for a few cases in our grid, although we do for most of them. For our fiducial subhaloes (Table 2) there is always a significant reduction of luminosity, the subhalo retaining about 15 per cent and 2 per cent of its initial luminosity in the non-baryonic

[7] Note that this actually corresponds to the annihilation luminosity in the case of a velocity-independent annihilation cross-section. If a velocity dependence was included, additional factors may come in.

[8] The fraction of lost particles within the innermost 1 per cent of the subhalo initial radius depends on the specs of the particular run, reaching up to ∼80 per cent in some cases.

[9] We noticed that a spike arises right before several pericentric passages for some runs. After performing some checks, we do find a fast increase of the subhalo density profile in the intermediate region $10^{-2} < x < 10^{-1}$. This L enhancement around the pericentric passage is induced by tidal compression. At the same time, kinetic energy is injected into the subhalo and it expands after passing the pericentre, inducing the density reduction for a short time. These processes are physical and the evolution of the density profile is numerically converged.

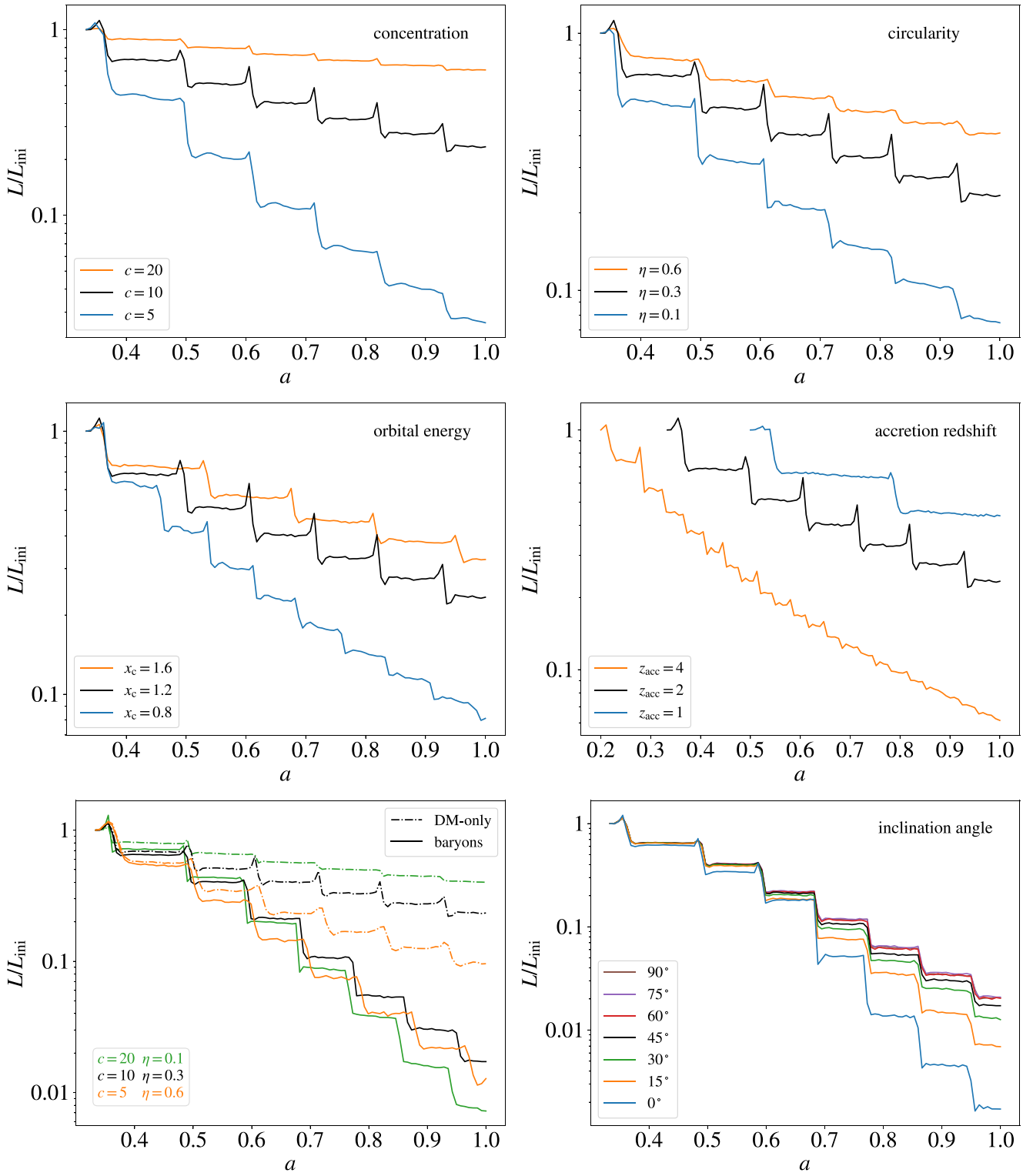

Figure 9. Evolution of the annihilation luminosity normalized to its initial value at accretion, L/L_{ini}, as a function of the scale factor, $a = 1/(1 + z)$, for different subhalo configurations. In each panel (except for the lower left), we vary one single parameter with respect to the fiducial set-up in Table 2. The latter corresponds to the black solid line in all panels. Comparison for different initial subhalo concentrations, c (upper left); different initial circularities, η (upper right); orbital energies, x_c (middle left); accretion redshifts, z_{acc} (middle right); comparison for runs with and without baryons (lower left); and different orbit inclination angles for the baryonic case (lower right).

and baryonic cases, respectively. More in general, it can be seen that the concentration is the most relevant parameter when baryons are not considered, the subhalo not losing a significant luminosity fraction when c is large enough, while also η plays a major role when baryons are added to the game. More specifically, baryons have a large impact on the annihilation luminosity when the orbits are more radial (smaller η) since the subhalo gets closer to the host halo centre, where baryons are mostly located, thus enhancing the disruption. This is more clearly visible in the bottom right-hand panel of the same Fig. 5, which shows the ratio between annihilation luminosities found at $z = 0$ in the baryonic and DM-only cases. The largest differences are located in the lower left area for the lowest c and η values considered. But still on the bottom right corner, where c is large but η is small, this ratio reaches values ∼0.3. In contrast, the ratio for $c = 5$ and $\eta = 0.8$ is ∼0.5 (upper left corner of the plot). When both c and η are large (upper right), both values are similar.

4 DISCUSSION

In this section, we try to simplify the parameter space of tidal stripping by summarizing it into a single parameter. First, in Section 4.1, we show that most dependence of the mass-loss on orbital parameters can be summarized through its dependence on the pericentre radius of the orbit. As a further simplification, we show in Section 4.2 that baryonic and DM-only cases follow the same relation when the pericentre tidal field is considered as the primary parameter instead, and further that also the concentration dependence can be explained by defining a single effective tidal field parameter that takes into account the structure-tide degeneracy (Stücker et al. 2022).

4.1 On the pericentres

While it is necessary to know the exact orbital configuration of a subhalo and the exact potential structure of the host to make an exact prediction of its mass-loss, good approximate predictions can still be obtained only through knowledge of a small subset of the parameters. Here, we try to understand what the single most predictive parameter for estimating the mass-loss is. First, we investigate the orbital pericentre as a candidate which has been proposed by several other studies (Peñarrubia et al. 2010; Drakos, Taylor & Benson 2020).

In the top panel of Fig. 10, we show f_b at present time as a function of the pericentre of the orbit[10] for different orbital parameters and accretion redshifts, We adopt $c = 10$ in all cases. Our results show that these points are roughly aligned in log–log space:

$$f_b = e(r_{peri}/r_{200,host})^m, \quad (8)$$

where $r_{peri}/r_{200,\,host}$ is the value of the pericentre in each case, i.e. the minimum distance between the subhalo and the host in each simulation, in terms of the virial radius of the host at $z = 0$. Our best-fitting parameters for those data, for both the non-baryonic and baryonic cases, are listed in Table 4. The corresponding fits are also shown in the top panel of Fig. 10 together with their respective scatter.

As expected, a smaller pericentre induces a larger mass-loss in general. This effect is much greater when baryons are taken into account, since they strongly enhance the tidal field in the centre of the host. Interestingly, the scatter is significant in both cases, with

[10]To be precise, among all pericentres since accretion, we select the one with the minimum distance to the host halo centre. Some small variations are indeed observed among pericentres in the same run, of the order of 10–20 per cent.

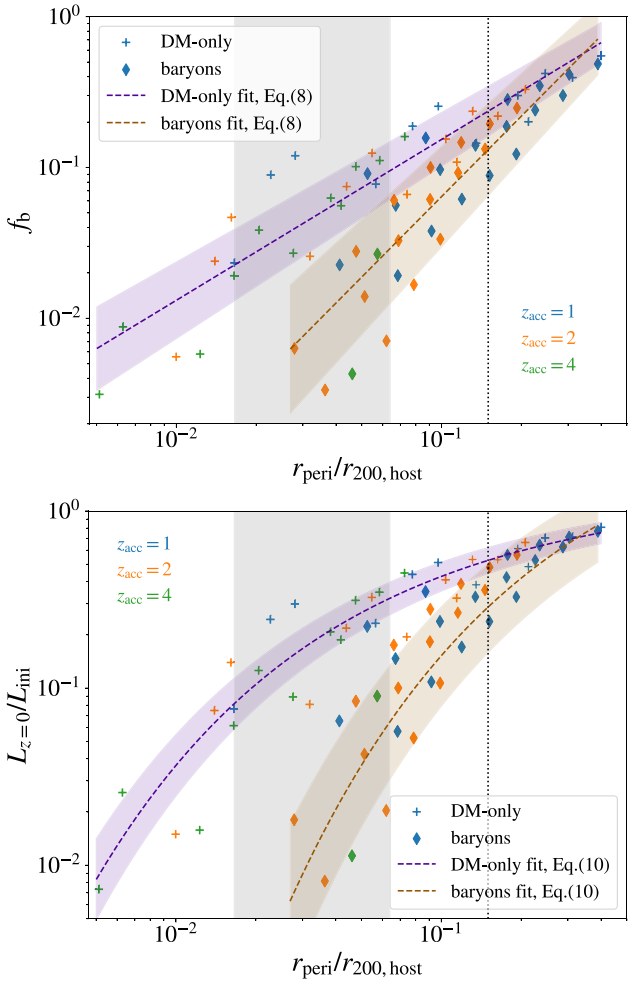

Figure 10. Top: bound mass fraction at present time as a function of the subhalo pericentric distance in units of the host virial radius at $z = 0$, $r_{peri}/r_{200,\,host}$, as found in different runs with an initial subhalo concentration $c = 10$. Each point corresponds to different orbital parameters and accretion redshifts. The dashed purple and brown lines correspond to fits to equation (8) using the best-fitting parameters collected in Table 4 for both the cases without and with baryons, respectively. Bottom: annihilation luminosity at present time, normalized to the initial one, as a function of the subhalo pericentric distance in units of the host virial radius, $r_{peri}/r_{200,\,host}$, as found in different runs with an initial subhalo concentration $c = 10$ and varying the orbital parameters and accretion redshifts. The dashed purple and brown lines correspond to fits to equation (10) using the best-fitting parameters collected in Table 4 for both the cases without and with baryons, respectively. In both panels, the grey area corresponds to the solar vicinity, defined as the Galactocentric region within 8.5 ± 5 kpc. The black dotted line shows the radius at which the baryonic tidal field is comparable to the DM halo one; see discussion in Section 4.1 and Fig. 11.

Table 4. Best-fitting parameters and uncertainties for the power-law function relating the pericentres with f_b, given by equation (8), and for the function relating the pericentres and $L_{z=0}/L_{ini}$, described in equation (10), both for the cases without and with baryons. These fits are for a particular value of concentrations, namely $c = 10$, and are shown in Fig. 10 together with the data used to perform the fits. See Section 4.1 for details.

	Without baryons	With baryons
m	1.07 ± 0.07	1.77 ± 0.16
$\log_{10}e$	0.25 ± 0.10	0.58 ± 0.17
n	1.43 ± 0.04	3.0 ± 0.4
d	1.3 ± 0.1	5 ± 1

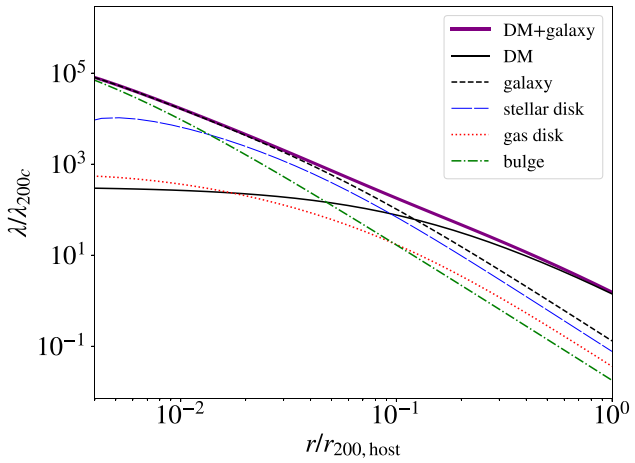

Figure 11. Values of the largest eigenvalue of the pericentric tidal field at $z = 0$ for the different components with respect to the distance to the host centre, normalized to the host virial radius. We are measuring tidal fields in units of λ_{200}, i.e. the tidal field that is necessary to create a saddle point in an NFW potential at r_{200} at redshift $z = 0$; see equation (9) for details.

ranges 0.13–0.29 and 0.54–0.85 dex for the DM-only and baryonic cases, respectively. This suggests that, even if the pericentric distance is the driving effect in the mass-loss, there are other, second-order effects also present in the process. It is also worth mentioning that we do not have points for small pericentric distances for the case of including baryons because of the lack of resolution, i.e. these points would lie below our convergence criteria.

Notice that both the non-baryonic and baryonic cases agree when the pericentre is sufficiently large. To get a better understanding of this behaviour, we need to introduce the notion of tidal field. We consider the tidal tensor, **T**, which has three eigenvalues. The largest of them, λ, is the most relevant one for our purposes, while the other two might just introduce second-order corrections. Fig. 11 shows the tidal field in units of[11]

$$\lambda_{200c} = \frac{\partial_r \phi_{\mathrm{NFW}}(r_{200})}{r_{200}} = 100 H_0^2, \tag{9}$$

where H_0 is the Hubble parameter at redshift $z = 0$, as a function of the normalized distance with respect to the host centre. We can see that the tidal field due to baryons is not relevant anymore for $r/r_{200,\,\mathrm{host}} \gtrsim 0.2$, since as said they are mostly located in the centre of the host. This explains that results in Fig. 10 for both the DM-only and baryonic cases are similar for large pericentric distances.

We have done the same analysis for the annihilation luminosity. The bottom panel of Fig. 10 shows its value at present time normalized to the initial one versus the pericentre of the orbit. We used the same runs that were used for the top panel of the same figure. From this exercise we can estimate the luminosity loss of subhaloes in the solar vicinity, depicted as a grey shaded region in the bottom panel of Fig. 10. In particular, if we only consider DM inside the host, subhaloes lose between 70 and 90 per cent of their initial L. When we add baryons, this percentage can increase up to 99 per cent.

We did not find a power-law behaviour in this case. We propose the following fitting function:

$$L_{z=0}/L_{\mathrm{ini}} = d \cdot n^{-1/\sqrt{r_{\mathrm{peri}}/r_{200,\mathrm{host}}}}. \tag{10}$$

[11] λ_{200c} is the tidal field that is necessary to introduce a saddle point in an NFW potential at r_{200} at redshift $z = 0$.

Our best-fitting parameters are also listed in Table 4. In this case, we observe again that both DM-only and baryonic results converge for large pericentric distances.

While it is intriguing to see that mass-loss and luminosity follow simple relations as a function of the pericentre radius, we want to emphasize here that the obtained relations will additionally depend on the initial concentration of the subhalo and on parameters that modify the host potential.

4.2 Mass-loss and the pericentre tidal field

As we have seen in Fig. 10, the pericentre versus mass-loss relation is different for host potentials that consider baryons and those which do not. This makes sense since tidal fields are much stronger in the host centre in the baryonic cases than in the DM-only case.

In Stücker et al. (2022), we have proposed that both of these cases may be unified into a single relation if we consider their pericentre tidal fields instead of their radii as the important parameters. Additionally, we have proposed in Stücker et al. (2022) that the concentration dependence of the tidal stripping problem should additionally disappear if we measure tidal fields in units of the scale tide λ_s and masses in units of the scale mass M_s:

$$M_s = \frac{\ln(2) - 1/2}{\ln(1+c) - c/(1+c)} M_{200}, \tag{11}$$

$$\lambda_s = \frac{\ln(2) - 1/2}{\ln(1+c) - c/(1+c)} c^3 \lambda_{200}. \tag{12}$$

In Stücker et al. (2022), we have developed a simple model that describes NFW haloes that are exposed to a tidal field, the latter increasing so slowly that the halo responds adiabatically. In the adiabatic limit (and assuming an isotropic tidal field), M_b/M_s, where M_b is the remaining mass in such limit, is exactly only a function of the effective tidal field, λ/λ_s. Now, in realistic set-ups many additional dependencies exist, but we would still expect that at first order most of the host potential dependence and most of the concentration dependence should disappear if results are presented in this way. Here, we want to test this expectation.

We measure the three eigenvalues $\lambda_1 \geq \lambda_2 \geq \lambda_3$ of the tidal tensor that the subhalo is exposed to at each time-step. Then, we infer the maximum value of λ_1 among all of the time-steps and we define this value as the pericentre tidal field, λ_{peri}.[12] Using the maximum of the tidal field as λ_{peri} has the advantage that it is always well defined even in cases of anisotropic or evolving host potentials, etc.

We show the mass-loss M/M_s as a function of $\lambda_{\mathrm{peri}}/\lambda_s$ in the top panel of Fig. 12, where we have combined runs with different concentrations, orbital parameters, and accretion redshifts, both with and without baryons. Strikingly, the cases with and without baryons follow the same relation when shown in this manner. This shows that the largest encountered tidal field is indeed the single most important parameter for understanding tidal mass-loss. Of course, there is a sizeable scatter in the relation, which shows that secondary dependencies exist.[13] Yet, the relation is now considerably tighter than the one shown in the top panel of Fig. 10. In the same top panel of

[12] We note that, in the baryonic case and because of the Galactic disc, this maximum tidal field may be reached at a point that does not exactly correspond to the actual pericentre, yet it will be typically very close.

[13] In particular, we noticed that (i) x_c is the driving parameter producing the vertical scatter, in such a way that for the same pericentric distance, different x_c values give a significantly different mass-loss even for the same values of η; (ii) the horizontal scatter is explained since subhaloes in more circular orbits and with a small x_c are closer to the host centre for longer times compared

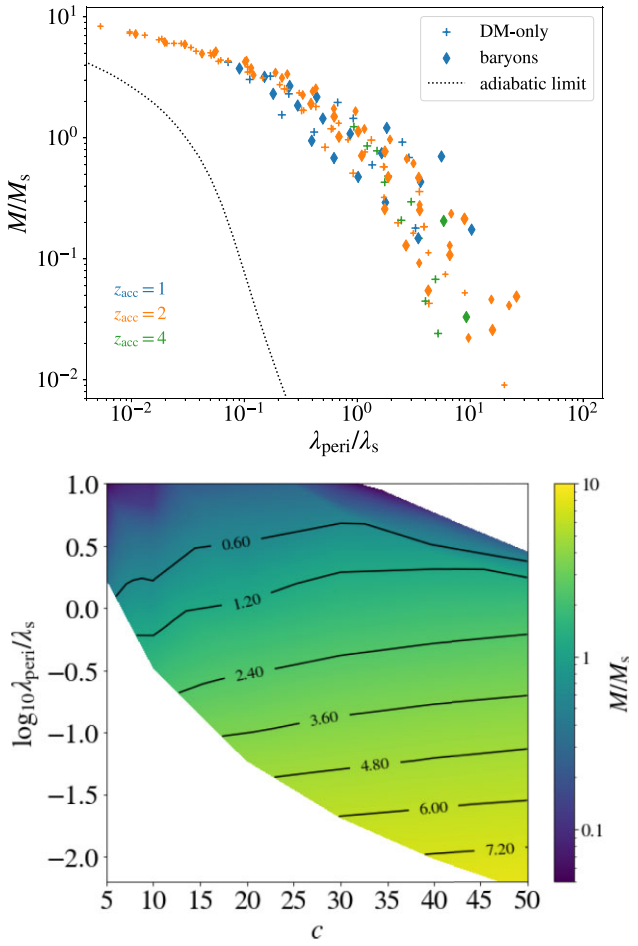

Figure 12. Top: subhalo mass at present divided by the initial scale mass (equation 11), as a function of the effective tide, i.e. the largest tidal tensor eigenvalue at the pericentre divided by the scale-tide λ_s (equation 12), for different subhalo concentrations (for $z_{acc} = 2$), redshifts (for $c = 10$), and orbital parameters, both with (diamonds) and without (plus signs) baryons. The dotted line is the adiabatic limit of Stücker et al. (2022), which represents the absolute maximum mass-loss expected after an infinite number of orbits. Bottom: remaining subhalo mass at present time divided by the scale mass, for different concentrations and effective tides at the pericentre. Iso-contours are now almost horizontal in contrast to those in Fig. 5. Note that both the bottom left and top right corners are in blank because they cannot be populated with our simulation suite (described in Table 2).

Fig. 12, we show a line corresponding to the adiabatic limit of Stücker et al. (2022), which represents the absolute maximum expected mass-loss in this parameter space. We note that our measured values here still lie quite far from the adiabatic limit. This is expected, as these subhaloes have orbited for much shorter times than what is necessary to reach the mentioned limit. Additionally, we may be overestimating the pericentre tidal field here a bit, by taking the maximum across the full history.

In the bottom panel of Fig. 12, we show the mass-loss as a function of the effective tide and concentration. When presented in these reduced units, the concentration dependence indeed disappears, i.e. the iso-contours in this plot are approximately horizontal. This shows that much of the parameter space of the tidal mass-loss problem can be simplified and generalized. The dependence on the initial concentration is degenerate with the dependence on the amplitude of the tidal field and we can summarize these two into one effective parameter λ_{peri}/λ_s – we call this phenomenon the 'structure-tide' degeneracy and we explain in Stücker et al. (2022) how this arises from the invariance of the Vlasov–Poisson system to time-rescalings. Note that we are not able to populate the lower left corner of this surface plot (bottom panel of Fig. 12), since we cannot reach such low values of the effective tide for small concentrations with the orbital configurations we are allowing in this work. A similar situation occurs for large tidal fields and concentrations.

The adiabatic limit prediction of this plot can be seen in the top left-hand panel of fig. 14 in Stücker et al. (2022). Again, we note that the scenarios considered here have lost much less mass than the adiabatic limit in Stücker et al. (2022), as expected (see explanation above).

5 CONCLUSIONS

Cosmological *N*-body simulations are computationally expensive and they are prone to both mass and spatial resolution limits, which makes it very difficult to properly resolve subhaloes and follow their evolution within their hosts. In contrast, employing an analytical prescription when modelling the host halo potential gives plenty of room to simulate a subhalo and to track its evolution with great accuracy and numerical resolution.

This work uses DASH, a code specifically designed to perform this task with unprecedented accuracy, reaching solar-mass and sub-parsec resolution in our simulations. In particular, in this work we have implemented a few important novelties with respect to the original version in Ogiya et al. (2019), which have made our results more realistic and useful. The most relevant ones are the inclusion of the evolution of the DM host potential; the implementation of the baryonic potential, which also evolves with time; and a new routine to select those orbital parameters that lead to a greater probability for a subhalo to cross the solar Galactocentric radius, i.e. those potentially most relevant for DM searches.

We have studied the evolution of subhaloes in an MW potential, the latter described as an NFW DM halo plus three baryonic components (stellar and gas discs, and bulge). We have explored different subhalo configurations, adopting a fiducial set of parameters as the representative case, but also varying one or some of these parameters to understand the role of each of them in the evolution of the subhalo. We have focused on studying two quantities particularly relevant for our purposes, the bound mass fraction and the DM annihilation luminosity. We have also performed several important convergence checks that allow us to confidently derive robust conclusions. Our main findings can be summarized as follows:

(i) Contrary to Kelley et al. (2019) and Grand & White (2021), we find that subhaloes do survive in the innermost 15 kpc of our Galaxy, although they typically lose more than 90 per cent of their initial masses (see top panel of Fig. 10).

(ii) Subhaloes with lower concentrations and subhaloes on orbits with smaller pericentric distances are more depleted. Similarly, subhaloes accreted earlier or with lower orbital energies have smaller orbits and have lost more mass at $z = 0$. This is illustrated, e.g. in Fig. 4. Including baryonic material in the host induces a significantly larger mass-loss in most cases as well, e.g. an order of magnitude more in the fiducial case (see e.g. left bottom panel of Fig. 5).

(iii) Subhaloes in parallel orbits with respect to the Galactic disc lose significantly more material than those orbiting in more

to subhaloes in radial orbits with large x_c values: the former ones have larger pericentres but suffer the same mass-loss in the end.

perpendicular orbits, similarly to that found in Green et al. (2021). Yet, the latter still lose significantly more mass than subhaloes orbiting a DM-only host. We also report more substantial mass-loss for parallel orbits compared to Green et al. (2021); see the right-hand panel of Fig. 6. Indeed, our results suggest that the relevance of disc shocking may be negligible compared to the undergoing baryonic tidal field during the whole evolution of the subhalo.

(iv) Subhaloes orbiting a DM-only halo with a pericentre in the solar vicinity have lost 70–90 per cent of their initial annihilation luminosity at $z = 0$. This percentage increases up to 99 per cent when baryons are included in the host (bottom panel of Fig. 10). In other words, we expect nearby low-mass subhaloes to be around 10 times less luminous with respect to those in DM-only.

(v) We emphasize that our results are virtually independent of subhalo mass for subhaloes lighter than 10^8 $M_\odot$ (Fig. 6). This was already stated by Ogiya et al. (2019) for the DM-only case and it is now confirmed for the baryonic scenario as well.

(vi) We have found new ways of summarizing the most important dependencies on the parameter space into a single parameter. First, we have found that the orbital dependence of subhalo mass-loss can be summarized at first order into its dependence on the pericentre radius. We have found simple power-law relations for a $c = 10$ subhalo that orbits in a Milky-Way-like host – with different relations for baryonic and DM-only cases. We note that these relations are not general though, but rather hold only for the specific concentration $c = 10$ that we investigated.

(vii) Motivated by the analytical arguments of Stücker et al. (2022), we have additionally found that the problem can be further simplified, by summarizing the concentration and host-potential dependence into the single parameter λ/λ_s – the effective tidal field at pericentre. The host-potential dependence (e.g. baryons versus DM-only) is captured, using the pericentre tidal field instead of the pericentre radius, since the tidal field is ultimately the cause of the mass-loss. Further, the concentration dependence is captured, by normalizing to the scale tide λ_s which depends on the concentration and is degenerate in its effects with the amplitude of the tidal field λ. We refer to this as the 'structure-tide' degeneracy and explain in Stücker et al. (2022) how it naturally arises from the time-rescaling invariance of the Vlasov–Poisson system.

Studying subhalo survival is crucial to elucidate the role of small subhaloes in indirect DM searches, which was one of the key motivations to perform this work. Among potential future applications of our work we can mention, for instance, a more refined calculation of the so-called subhalo boost factor to annihilation signals, more robust constraints on DM, especially for those scientific cases where subhaloes play a central role, and the optimization of DM search observation strategies for spatially extended DM targets. Regarding the boost in particular, we can already anticipate that, since we find most of our subhaloes to survive the tidal forces they are subject to, and since many of these subhaloes can exist in the solar vicinity, the annihilation signal will be boosted indeed (e.g. Moliné et al. 2017; Stref & Lavalle 2017; Ibarra, Kavanagh & Rappelt 2019; Facchinetti, Lavalle & Stref 2020). Further work is needed though to accurately compute this factor, as we expect it to be not as high as most of these works may suggest. We recall that, according to our findings, in many cases the mass that subhaloes are able to retain is confined in a radius much smaller than the formal tidal radius, which is the one typically used for the calculations of the boost.

This work is still ongoing. In the near future, we will take a closer look at the evolution of the subhalo concentration with time, as well as the impact of the latter for indirect DM searches. We would also like to understand the impact of our findings on both the radial distribution and mass function of the MW subhalo population. Besides, we are considering running more massive simulations with higher resolution, which will allow to track f_b for more extreme c cases, as well as calculating the annihilation luminosity with higher confidence.

ACKNOWLEDGEMENTS

The work of AAS and MASC was supported by the grants PGC2018-095161-B-I00 and CEX2020-001007-S, both funded by MCIN/AEI/10.13039/501100011033 and by 'ERDF A way of making Europe'. The work of AAS was also supported by the Spanish Ministry of Science and Innovation through the grant FPI-UAM 2018. MASC was also supported by the Atracción de Talento contract no. 2020-5A/TIC-19725 granted by the Comunidad de Madrid in Spain. GO was supported by the Fundamental Research Fund for the Central Universities (Grant No. NZ2020021) and the Waterloo Centre for Astrophysics Fellowship. JS and RA acknowledge the support of the European Research Council through grant number ERC-StG/716151 (BACCO).

Our simulations were carried out in the Atlas and Graham supercomputers, operated by the DIPC and Compute Canada (www.computecanada.ca), respectively.

This research used Python, along with community-developed or maintained software packages, including IPYTHON (Perez & Granger 2007), MATPLOTLIB (Hunter 2007), NUMPY (van der Walt, Colbert & Varoquaux 2011), and SCIPY (Virtanen et al. 2020).

DATA AVAILABILITY

The data underlying this article will be shared on reasonable request to the corresponding author.

REFERENCES

Achterberg A. et al., 2006, Astropart. Phys., 26, 155
Ackermann M. et al., 2012, ApJ, 747, 121
Ackermann M. et al., 2015, Phys. Rev. Lett., 115, 231301
Aghanim N. et al., 2020, A&A, 641, A6
Amorisco N. C., 2021, preprint (arXiv:2111.01148)
Ando S., Ishiyama T., Hiroshima N., 2019, Galaxies, 7, 68
Angulo R. E., Hahn O., 2022, Living Rev. Comput. Astrophys., 8, 1
Angulo R. E., Baugh C. M., Frenk C. S., Lacey C. G., 2014, MNRAS, 442, 3256
Barnes J., Hut P., 1986, Nature, 324, 446
Battiston R., 2008, Nucl. Instrum. Methods A, 588, 227
Behroozi P., Wechsler R. H., Hearin A. P., Conroy C., 2019, MNRAS, 488, 3143
Bertone G., Hooper D., 2018, Rev. Mod. Phys., 90, 045002
Bertone G., Merritt D., 2005, Mod. Phys. Lett. A, 20, 1021
Bertone G., Hooper D., Silk J., 2005, Phys. Rept., 405, 279
Binney J., Tremaine S., 2008, Galactic Dynamics: Second Edition. Princeton University Press
Bullock J. S., Kravtsov A. V., Weinberg D. H., 2000, ApJ, 539, 517
Chandrasekhar S., 1943, ApJ, 97, 255
Coronado-Blázquez J., Sánchez-Conde M. A., Domínguez A., Aguirre-Santaella A., Mauro M. D., Mirabal N., Nieto D., Charles E., 2019a, J. Cosmol. Astropart. Phys., 2019, 020
Coronado-Blázquez J., Sánchez-Conde M. A., Mauro M. D., Aguirre-Santaella A., Ciucă I., Domínguez A., Kawata D., Mirabal N., 2019b, J. Cosmol. Astropart. Phys., 2019, 045
Coronado-Blázquez J., Doro M., Sánchez-Conde M. A., Aguirre-Santaella A., 2021, Phys. Dark Universe, 32, 100845

Coronado-Blázquez J., Sánchez-Conde M. A., Pérez-Romero J., Aguirre-Santaella A., Fermi-LAT Collaboration, 2022, Phys. Rev. D, 105, 083006
Correa C. A., Wyithe J. S. B., Schaye J., Duffy A. R., 2015, MNRAS, 450, 1521
D'Onghia E., Springel V., Hernquist L., Keres D., 2010, ApJ, 709, 1138
Diemand J., Kuhlen M., Madau P., 2007, ApJ., 667, 859
Diemand J., Kuhlen M., Madau P., Zemp M., Moore B., Potter D., Stadel J., 2008, Nature, 454, 735
Drakos N. E., Taylor J. E., Benson A. J., 2020, MNRAS, 494, 378
Eddington A. S., 1916, MNRAS, 76, 572
Errani R., Peñarrubia J., 2020, MNRAS, 491, 4591
Facchinetti G., Lavalle J., Stref M., 2020, preprint (arXiv:2007.10392)
Fattahi A. et al., 2016, MNRAS, 457, 844
Flix J., MAGIC Collaboration, 2004, in Prada F., Martinez Delgado D., Mahoney T. J., eds, ASP Conf. Ser. Vol. 327, Satellites and Tidal Streams. Astron. Soc. Pac., San Francisco, p. 52
Flynn C., Sommer-Larsen J., Christensen P. R., 1996, MNRAS, 281, 1027
Frenk C. S., White S. D. M., 2012, Ann. Phys., Lpz., 524, 507
Garrett K., Duda G., 2011, Adv. Astron., 2011, 968283
Garrison-Kimmel S. et al., 2017, MNRAS, 471, 1709
Gehrels N., Michelson P., 1999, Astropart. Phys., 11, 277
Grand R. J. J., White S. D. M., 2021, MNRAS, 501, 3558
Grand R. J. J. et al., 2021, MNRAS, 507, 4953
Green S. B., van den Bosch F. C., 2019, MNRAS, 490, 2091
Green S. B., van den Bosch F. C., Jiang F., 2021, MNRAS, 509, 2624
Hayashi E., Navarro J. F., Taylor J. E., Stadel J., Quinn T., 2003, ApJ, 584, 541
Hernquist L., 1990, ApJ, 356, 359
Hiroshima N., Ando S., Ishiyama T., 2018, Phys. Rev. D, 97, 123002
Hinton J. A., HESS Collaboration, 2004, New Astron. Rev., 48, 331
Hooper D., Witte S. J., 2017, J. Cosmol. Astropart. Phys., 2017, 018
Hunter J. D., 2007, Comput. Sci. Eng., 9, 90
Ibarra A., Kavanagh B. J., Rappelt A., 2019, J. Cosmol. Astropart. Phys., 2019, 013
Ishiyama T. et al., 2021, MNRAS, 506, 4210
Jiang L., Cole S., Sawala T., Frenk C. S., 2015, MNRAS, 448, 1674
Kahlhoefer F., 2017, Int. J. Mod. Phys. A, 32, 1730006
Kelley T., Bullock J. S., Garrison-Kimmel S., Boylan-Kolchin M., Pawlowski M. S., Graus A. S., 2019, MNRAS, 487, 4409
Ludlow A. D., Bose S., Angulo R. E., Wang L., Hellwing W. A., Navarro J. F., Cole S., Frenk C. S., 2016, MNRAS, 460, 1214
Melott A. L., Shandarin S. F., Splinter R. J., Suto Y., 1997, ApJ, 479, L79
Miller T. B., van den Bosch F. C., Green S. B., Ogiya G., 2020, MNRAS, 495, 4496
Miyamoto M., Nagai R., 1975, PASJ, 27, 533
Moliné A., Sánchez-Conde M. A., Palomares-Ruiz S., Prada F., 2017, MNRAS, 466, 4974
Navarro J. F., Frenk C. S., White S. D. M., 1997, ApJ, 490, 493
Navarro J. F. et al., 2010, MNRAS, 402, 21
Ogiya G., Mori M., Miki Y., Boku T., Nakasato N., 2013, in Journal of Physics Conference Series. p. 012014
Ogiya G., van den Bosch F. C., Hahn O., Green S. B., Miller T. B., Burkert A., 2019, MNRAS, 485, 189
Ogiya G., Taylor J. E., Hudson M. J., 2021, MNRAS, 503, 1233
Okamoto T., Gao L., Theuns T., 2008, MNRAS, 390, 920
Okoli C., Taylor J. E., Afshordi N., 2018, J. Cosmol. Astropart. Phys., 2018, 019
Peñarrubia J., Benson A. J., Walker M. G., Gilmore G., McConnachie A. W., Mayer L., 2010, MNRAS, 406, 1290
Perez F., Granger B. E., 2007, Comput. Sci. Eng., 9, 21
Picozza P. et al., 2007, Astropart. Phys., 27, 296
Plummer H. C., 1911, MNRAS, 71, 460
Popping G. et al., 2015, MNRAS, 454, 2258
Porter T. A., Johnson R. P., Graham P. W., 2011, ARA&A, 49, 155
Power C., Navarro J. F., Jenkins A., Frenk C. S., White S. D. M., Springel V., Stadel J., Quinn T., 2003, MNRAS, 338, 14
Press W. H., Teukolsky S. A., Vetterling W. T., Flannery B. P., 2002, Numerical recipes in C+ + : The Art of Scientific Computing, 2nd edition. Cambridge University Press
Romeo A. B., Agertz O., Moore B., Stadel J., 2008, ApJ, 686, 1
Sánchez-Conde M. A., Prada F., 2014, MNRAS, 442, 2271
Sawala T. et al., 2016, MNRAS, 457, 1931
Smith R., Flynn C., Candlish G. N., Fellhauer M., Gibson B. K., 2015, MNRAS, 448, 2934
Splinter R. J., Melott A. L., Shandarin S. F., Suto Y., 1998, ApJ, 497, 38
Springel V., 2005, MNRAS, 364, 1105
Springel V., Frenk C. S., White S. D. M., 2006, Nature, 440, 1137
Springel V. et al., 2008, MNRAS, 391, 1685
Stref M., Lavalle J., 2017, Phys. Rev. D, 95, 063003
Strigari L. E., 2013, Phys. Rep., 531, 1
Stücker J., Ogiya G., Angulo R. E., Aguirre-Santaella A., Sánchez-Conde M. A., 2022, preprint (arXiv:2207.00604)
van den Bosch F. C., Ogiya G., 2018, MNRAS, 475, 4066
van den Bosch F. C., Ogiya G., Hahn O., Burkert A., 2018, MNRAS, 474, 3043
van der Wel A. et al., 2014, ApJ, 788, 28
van der Walt S., Colbert S. C., Varoquaux G., 2011, Comput. Sci. Eng., 13, 22
Virtanen P., Gommers R., Oliphant T. E. et al., 2020, Nat. Methods, 17, 261
Vogelsberger M. et al., 2014, MNRAS, 444, 1518
Vogelsberger M., Marinacci F., Torrey P., Puchwein E., 2020, Nat. Rev. Phys., 2, 42
Weekes T. C. et al., 2002, Astropart. Phys., 17, 221
Wojtak R., Łokas E. L., Mamon G. A., Gottlöber S., 2009, MNRAS, 399, 812
Yang X., Mo H. J., Zhang Y., van den Bosch F. C., 2011, ApJ, 741, 13
Zavala J., Frenk C. S., 2019, Galaxies, 7, 81

APPENDIX A: A DEEPER LOOK INTO CONVERGENCE

A1 Bound mass fraction

We have taken into account two different numerical convergence criteria in order to elucidate whether the subhalo has been physically or numerically disrupted. The first one depends on the softening length, ε, and the second is related to the number of particles, N (van den Bosch & Ogiya 2018). The maximum among the two of these criteria for a given run is the one we finally adopt in each case. In particular:

$$f_{\rm b} > f_{\rm b}^{\rm min,1} = 1.12\frac{c^{1.26}}{f^2(c)}\left(\frac{\varepsilon}{r_{\rm s,0}}\right)^2$$
$$f_{\rm b} > f_{\rm b}^{\rm min,2} = 0.32\left(\frac{N_{\rm acc}}{1000}\right)^{-0.8}$$
$$f_{\rm b}^{\rm min} \equiv \max\left(f_{\rm b}^{\rm min,1}, f_{\rm b}^{\rm min,2}\right) \quad \text{(A1)}$$

We consider that the subhalo has been numerically disrupted and no robust conclusions can be obtained from that simulation if the bound mass fraction drops below that value before $z = 0$. We note though that this line lies always below 10^{-2}, i.e. the subhalo has already lost more than 99 per cent of its mass by then. None the less, this does not necessarily mean that the subhalo has been *physically* disrupted, but rather we do not have enough resolution to study accurately the mass-loss beyond.

These criteria in equation (A1) have been tested for runs without baryons in van den Bosch & Ogiya (2018). Here, we have verified that they still hold when the baryonic components are added to the host potential as well, by performing several simulations employing our default setting and changing the numerical parameters, N and ε.

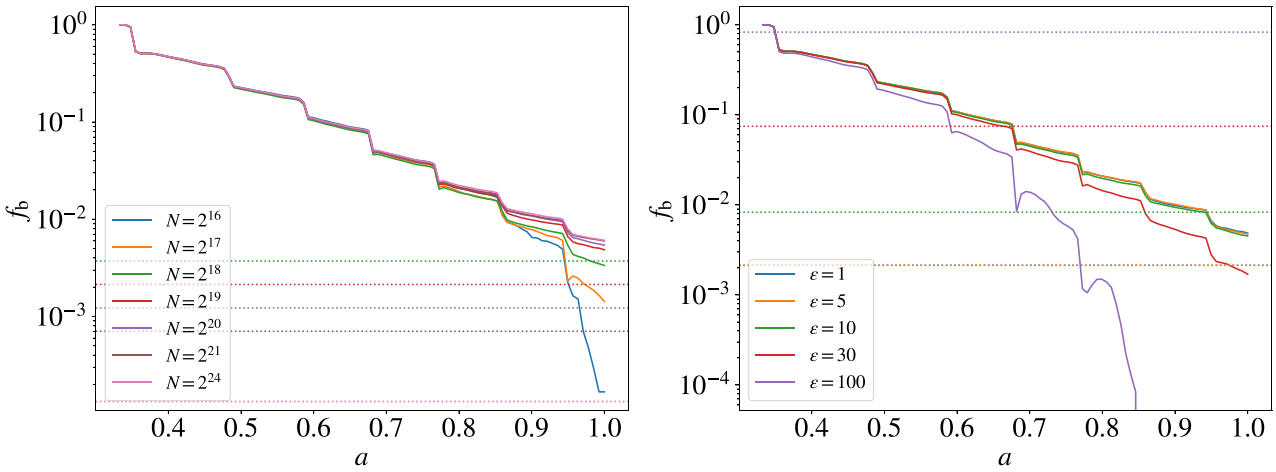

Figure A1. Convergence checks including baryons. Left-hand panel: bound mass fraction for different initial number of particles, N, together with their corresponding convergence limits, the latter depicted as horizontal dotted lines coloured according to the legend. Right-hand panel: bound mass fraction for different values of the softening length ε, where $\varepsilon_0 = 0.0003 \times r_{200,\,\mathrm{sub}} = 0.304$ pc in the legend. We adopt our fiducial set-up of Table 2 in all cases and the inclination angle is fixed to 45 deg in the baryonic runs.

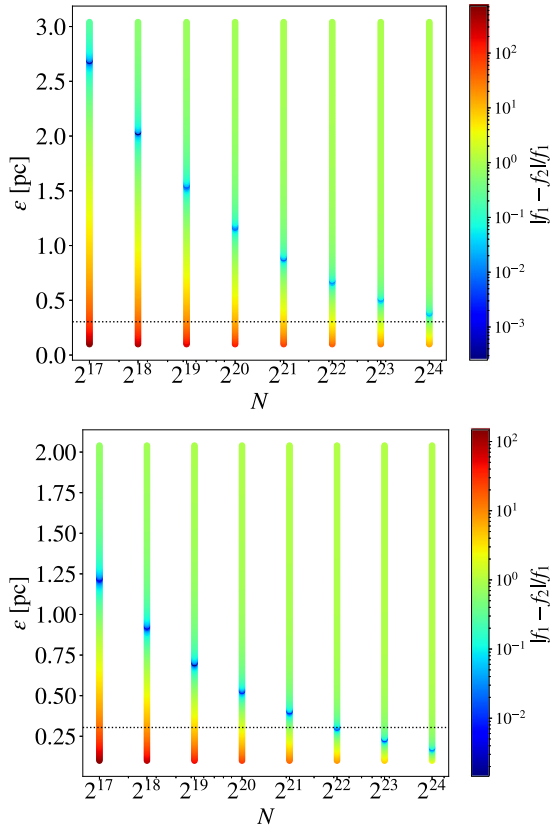

Figure A2. Ratio between both f_b convergence criteria in equation (A1), for different pairs $N - \varepsilon$ and for two initial subhalo concentrations, $c = 10$ (top) and $c = 20$ (bottom). The dotted line corresponds to our default ε for $z_{\mathrm{acc}} = 2$. See the text for details.

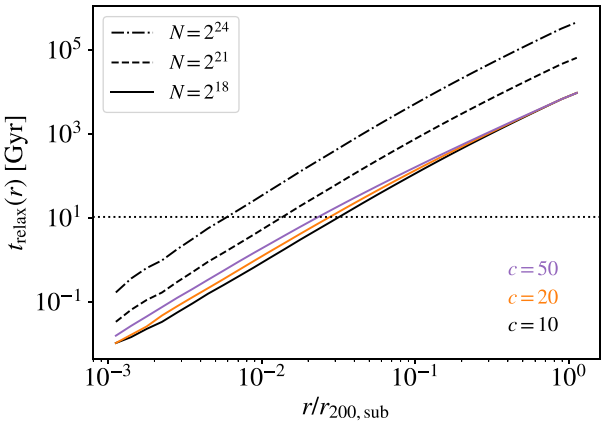

Figure A3. Relaxation time-scale for different concentrations and number of particles, using the initial snapshot for runs with $z_{\mathrm{acc}} = 2$, as a function of the normalized subhalo inner radius. The horizontal dotted black line corresponds to the time of the simulation, t_{sim}, and indicates the radius above which the simulation can be trusted.

The results are shown in Fig. A1, where we can see that the mass-loss is increased when either criterion is unsatisfied and that the criteria work nicely with baryons, too, since the results converge – within a small scatter – when they are above their respective convergence line. We have also found that increasing ε can result in less mass-loss even below the convergence line. This can be explained since the two-body relaxation time-scale also depends slightly on ε; the smaller the ε, the shorter the relaxation time-scale. We will discuss the effect of relaxation time-scale below.

It is important to realize that a larger N or a smaller ε costs more computational time. Choosing the optimal N and ε values for each simulation is a non-trivial but an important task, since we need to find a compromise between computational time and numerical resolution. Since the critical value of f_b is the maximum of the two criteria in equation A1, we can compute when these values are closer depending on our numerical parameters. We have plotted this relation between the criteria in Fig. A2 for two different concentration values, $c = 10$ and $c = 20$. We are only showing N values which are a power of 2 because we are using those in this work. The colourbar represents how close these values are, where the dark blue means they are the closest, i.e. a smaller difference between both criteria, which is optimal for our purposes. However, increasing N makes the optimal

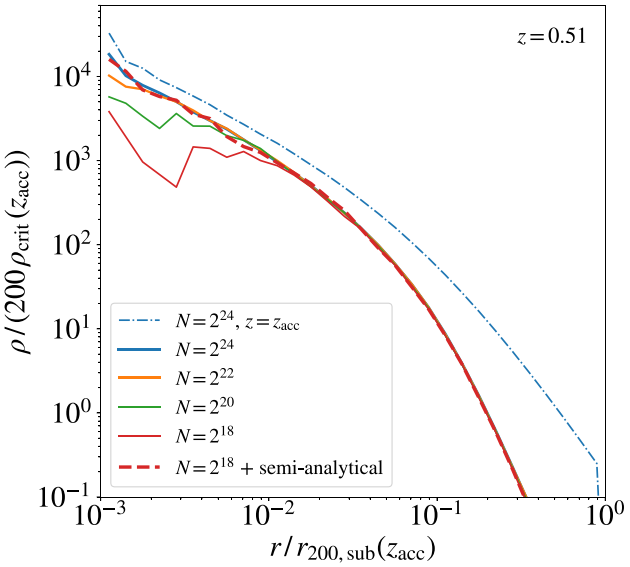

Figure A4. Example of subhalo DM density profile ρ, normalized to 200 times the critical density at accretion, after several pericentric passages for runs with a different total number of particles, N. The red dashed line corresponds to the hybrid, semi-analytical scheme we adopted to recover the cusp in low-resolution runs in order to save computational time; see Appendix A2 for details.

ε smaller. Therefore, the convergence value is not going to improve below the dark blue points. The same happens to the right.

In our work, we use a different number of particles depending on the case we are studying. On one hand, our N ranges from 2^{18} to 2^{21}. We have also studied the fiducial case with larger values of N, up to 2^{24}, to verify the convergence of our results. On the other hand, we are going to set $\varepsilon = 0.0003\, r_{200,\rm sub}$ from now on, which is good enough for our purposes.

As stated above, we also have to take into account the relaxation time-scale. When a system is described with a finite number of particles, the acceleration of each one eventually deviates from the mean value when particles get close to each other (Power et al. 2003; Binney & Tremaine 2008). These 'collisions' drive changes of order unity in energy on the relaxation time-scale, which is obtained as

$$t_{\rm relax} \simeq \frac{N(<r)}{8\ln N(<r)} t_{\rm cross}(r), \tag{A2}$$

where $t_{\rm cross}(r) = \frac{2\pi r}{V_{\rm c}(r)} = 2\pi\sqrt{\frac{r^3}{GM(r)}}$ is the crossing time, a rough estimation of the orbital period of a particle at r in the subhalo. After one relaxation time, the cumulative small kicks from many encounters with other particles have changed the particle's orbit significantly from the one it would have had if the gravitational field had been smooth, meaning the particle has lost its memory of its initial conditions when a relaxation time has passed. This implies that the larger the relaxation time, the more trustful the results obtained at the innermost parts. More specifically, we can trust a simulation at radius r if it satisfies $t_{\rm relax}(r) > t_{\rm sim}$, where $t_{\rm sim}$ depends on $z_{\rm acc}$. This relaxation time-scale is shown in Fig. A3 for different radii, subhalo concentrations, and number of particles, using the first snapshot in every case. It is slightly larger for a larger concentration or number of particles, which means we may need to use more particles when the concentration is smaller. More specifically, we can trust our data from $r/r_{200,\,\rm sub} \sim 5 \times 10^{-3}$ if $N = 2^{24}$ and $z_{\rm acc} = 2$ while, if $N = 2^{18}$, the simulations are believable only from $r/r_{200,\,\rm sub} \sim 3 \times 10^{-2}$. This will be particularly relevant when the subhalo experiences a significant mass-loss.

A2 Annihilation luminosity

As explained in Section 3.2, we are facing numerical resolution issues when studying the evolution of the innermost regions of the subhalo. Indeed, when N is not large enough, the subhalo inner cusp ends transforming into a core without any physical explanation. This can be seen in Fig. A4, where we show an example of a density profile for different values of N and our fiducial set of parameters, including baryons, some time after the subhalo has been accreted. For a considerably large number of particles, $N = 2^{24}$ in our case of study, we mostly recover a cusp in the subhalo centre, while this is not the case for a lower number of particles. Note that the subhalo gets truncated in its outskirts as it orbits around the host and loses mass, as physically expected, and this behaviour does not change for a lower resolution run.

Unfortunately, working with such large resolutions becomes unsuitable in terms of the computational cost. Because of this, we have implemented a hybrid approach to recover the inner cusp even in cases where the resolution is not sufficiently high. To do so, we first set a critical subhalo radius, $x_{\rm crit} = r_{\rm crit}/r_{200,\,\rm sub}$, the radius from which we can trust our results according to the relaxation time-scale for a given number of particles (see Appendix A1), and trust the simulation data only beyond that point ($x > x_{\rm crit}$). As for the innermost subhalo region, which we recall is of special relevance for our DM annihilation studies, we use the semi-analytical model in Green & van den Bosch (2019) to describe the evolution of the subhalo inner cusp with time, down to $x = 5 \times 10^{-3}$, which corresponds to the relaxation time-scale for the higher resolution we have tested, $N = 2^{24}$ particles. The red dashed line in Fig. A4 shows how this hybrid scheme fixes the internal part of the subhalo, giving a similar result as the high-resolution, 2^{24} particles run.

This paper has been typeset from a TEX/LATEX file prepared by the author.